

# The MOSDEF Survey: Environmental Dependence of the Gas-phase Metallicity of Galaxies at $1.4 \leqslant z \leqslant 2.6^*$

Nima Chartab 1 , Bahram Mobasher 1, Alice E. Shapley 2 , Irene Shivaei 3,10 , Ryan L. Sanders 4,10 , Alison L. Coil , Alice E. Shapley 2 , Irene Shivaei 3,10 , Ryan L. Sanders 4,10 , Alison L. Coil , Alice E. Shapley 2 , Irene Shivaei 3,10 , Ryan L. Sanders 4,10 , Alice E. Shapley 2 , Irene Shivaei 3,10 , Ryan L. Sanders 4,10 , Alice E. Shapley 2 , Irene Shivaei 3,10 , Ryan L. Sanders 4,10 , Alice E. Shapley 2 , Irene Shivaei 3,10 , Ryan L. Sanders 4,10 , Alice E. Shapley 2 , Irene Shivaei 3,10 , Ryan L. Sanders 4,10 , Alice E. Shapley 2 , Irene Shivaei 3,10 , Ryan L. Sanders 4,10 , Alice E. Shapley 2 , Irene Shivaei 3,10 , Irene S Mariska Kriek<sup>6</sup>, Naveen A. Reddy<sup>1</sup>, Brian Siana<sup>1</sup>, William R. Freeman<sup>1</sup>, Mojegan Azadi<sup>7</sup>, Guillermo Barro<sup>8</sup>, Tara Fetherolf<sup>1</sup>, Gene Leung<sup>5</sup>, Sedona H. Price<sup>9</sup>, and Tom Zick<sup>6</sup> Department of Physics and Astronomy, University of California, Riverside, 900 University Ave, Riverside, CA 92521, USA; nima.chartab@email.ucr.edu Department of Physics & Astronomy, University of California, Los Angeles, 430 Portola Plaza, Los Angeles, CA 90095, USA <sup>3</sup> Steward Observatory, University of Arizona, 933 North Cherry Ave, Tucson, AZ 85721, USA <sup>4</sup> Department of Physics and Astronomy, University of California, Davis, One Shields Ave, Davis, CA 95616, USA <sup>5</sup> Center for Astrophysics and Space Sciences, University of California, San Diego, 9500 Gilman Dr, La Jolla, CA 92093-0424, USA Astronomy Department, University of California, Berkeley, CA 94720, USA <sup>7</sup> Harvard-Smithsonian Center for Astrophysics, 60 Garden St, Cambridge, MA 02138, USA 8 Department of Physics, University of the Pacific, 3601 Pacific Ave, Stockton, CA 95211, USA <sup>9</sup> Max-Planck-Institut für extraterrestrische Physik, Postfach 1312, Garching, D-85741, Germany Received 2020 October 19; revised 2020 December 14; accepted 2020 December 27; published 2021 February 18

### Abstract

Using the near-IR spectroscopy of the MOSFIRE Deep Evolution Field survey, we investigate the role of the local environment in the gas-phase metallicity of galaxies. The local environment measurements are derived from accurate and uniformly calculated photometric redshifts with well-calibrated probability distributions. Based on rest-frame optical emission lines, [N II] $\lambda$ 6584 and H $\alpha$ , we measure gas-phase oxygen abundances of 167 galaxies at  $1.37 \leqslant z \leqslant 1.7$  and 303 galaxies at  $2.09 \leqslant z \leqslant 2.61$ , located in diverse environments. We find that at  $z \sim 1.5$ , the average metallicity of galaxies in overdensities with  $M_* \sim 10^{9.8} \, M_{\odot}$ ,  $10^{10.2} \, M_{\odot}$ , and  $10^{10.8} \, M_{\odot}$  is higher relative to their field counterparts by  $0.094 \pm 0.051$ ,  $0.068 \pm 0.028$ , and  $0.052 \pm 0.043$  dex, respectively. However, this metallicity enhancement does not exist at higher redshift,  $z \sim 2.3$ , where, compared to the field galaxies, we find  $0.056 \pm 0.043$ ,  $0.056 \pm 0.028$ , and  $0.096 \pm 0.034$  dex lower metallicity for galaxies in overdense environments with  $M_* \sim 10^{9.8} M_{\odot}$ ,  $10^{10.2} M_{\odot}$  and  $10^{10.7} M_{\odot}$ , respectively. Our results suggest that, at  $1.37 \leqslant z \leqslant 2.61$ , the variation of mass–metallicity relation with local environment is small (<0.1 dex), and reverses at  $z \sim 2$ . Our results support the hypothesis that, at the early stages of cluster formation, owing to efficient gas cooling, galaxies residing in overdensities host a higher fraction of pristine gas with prominent primordial gas accretion, which lowers their gas-phase metallicity compared to their coeval field galaxies. However, as the universe evolves to lower redshifts  $(z \le 2)$ , the shock-heated gas in overdensities cannot cool down efficiently, and galaxies become metal-rich rapidly due to the suppression of pristine gas inflow and re-accretion of metal-enriched outflows in overdensities.

Unified Astronomy Thesaurus concepts: Metallicity (1031); Galaxy environments (2029); Galaxy evolution (594); High-redshift galaxies (734); Large-scale structure of the universe (902)

### 1. Introduction

Over the last few years, we have made significant progress toward developing a comprehensive and self-consistent model for the formation of galaxies. At each step, however, the model is compounded by nonlinear effects regarding the feedback processes involved and the parameters driving them. Gas accretion from the intergalactic medium (IGM) supplies cold gas for a galaxy to build up its stellar population through the gravitational collapse of molecular clouds. As the stars form, heavy elements are produced in their hot cores, resulting in the chemically enriched material that will be expelled to the interstellar medium (ISM) through feedback processes such as stellar winds (Garnett 2002; Brooks et al. 2007) and/or supernovae explosions (e.g., Steidel et al. 2010; Martin et al. 2012; Chisholm et al. 2018). Furthermore, feedback processes can remove part of the enriched material from galaxies into the IGM (e.g., Heckman et al. 1990; Tremonti et al. 2004;

10 Hubble Fellow.

Chisholm et al. 2018). Thus, gas-phase metallicity is expected to be connected with most of the galaxy evolutionary processes (e.g., gas inflow/outflow and star formation) and can be considered as one of the fundamental characteristics of galaxies that encodes information regarding galaxy evolution over cosmic time.

A tight correlation has been observed between the gas-phase metallicity and stellar mass of galaxies (mass-metallicity relation, hereafter MZR) out to  $z \sim 3.5$ , such that galaxies with lower stellar masses have lower metallicities (e.g., Tremonti et al. 2004; Erb et al. 2006; Mannucci et al. 2009; Finkelstein et al. 2011; Steidel et al. 2014; Sanders et al. 2015, 2020). Moreover, it has been found that the MZR evolves with redshift so that galaxies at a given stellar mass have a lower metallicity at high redshifts (e.g., Steidel et al. 2014; Maiolino & Mannucci 2019; Sanders et al. 2020).

Although a tight correlation has been found between stellar mass and gas-phase metallicity spanning a wide range of stellar masses, other physical properties of galaxies could also contribute to the observed scatter in this relation. For example, the star formation rate (SFR) in a galaxy controls the metallicity. At a given stellar mass, galaxies with lower SFRs have higher metallicities (e.g., Mannucci et al. 2010;

<sup>\*</sup> Based on data obtained at the W.M. Keck Observatory, which is operated as a scientific partnership among the California Institute of Technology, the University of California, and NASA, and was made possible by the generous financial support of the W.M. Keck Foundation.

Sanders et al. 2018). Gas accretion from the IGM adds chemically poor gas into the ISM of a galaxy, which lowers the galaxy's gas-phase metallicity. On the other hand, cold gas infall that provides additional fuel for star formation increases the SFR. Therefore, cold gas accretion changes the metallicity content of the ISM in a complicated way. Lilly et al. (2013) introduced a gas regulator model that expresses the gas-phase metallicity of a galaxy in terms of the properties of the accreted gas (metallicity and rate of infalling gas) and SFR. Their model explains the observationally confirmed dependence of the MZR on SFR.

However, the evolution of the ISM and its metal content does, to a large extent, depend on the properties of the infalling gas that, in turn, is affected by the environment where the galaxy resides (Peng & Maiolino 2014; Gupta et al. 2018). Chartab et al. (2020) studied the environmental dependence of star formation activity of galaxies in the five widely separated fields of the Cosmic Assembly Near-IR Deep Extragalactic Legacy Survey (CANDELS; Grogin et al. 2011; Koekemoer et al. 2011) out to  $z \sim 3.5$ . They found that environmental quenching efficiency evolves with stellar mass such that massive galaxies in overdense regions become quenched more efficiently than their low-mass counterparts. This suggests that, besides the stellar mass quenching, which is the dominant quenching mechanism at high redshift, the environmental quenching is also effective as early as  $z \sim 3$  for massive galaxies (i.e., the quiescent fraction of galaxies with  $M_* \sim 10^{11} M_{\odot}$  are 20% higher (Chartab et al. 2020) in overdensities than that of field counterparts at  $z \sim 2.8$ ). They also suggest that the growth of environmental quenching efficiency with stellar mass can be explained by the termination of cold gas accretion in an overdense environment. In the absence of cold gas accretion, massive galaxies exhaust their remaining gas reservoirs in shorter timescales compared to lowmass galaxies (also see Balogh et al. 2016; Fossati et al. 2017; Kawinwanichakij et al. 2017; Old et al. 2020). Using the Evolution and Assembly of GaLaxies and their Environments simulation, van de Voort et al. (2017) found a suppression of the cold gas accretion rate in dense environments, mostly for satellite galaxies. Zavala et al. (2019) reported Atacama Large Millimeter/submillimeter Array observations of 68 spectroscopically confirmed galaxies within two protoclusters at  $z \sim 2.2$  and found that protoclusters contain a higher fraction of massive and gas-poor galaxies compared to those residing in the field environment. They concluded that the environmental quenching exists during the early phases of cluster formation (also see Darvish et al. 2016; Nantais et al. 2017; Ji et al. 2018; Pintos-Castro et al. 2019; Ando et al. 2020; Contini et al. 2020). However, Lemaux et al. (2020) recently observed an enhanced star formation for star-forming galaxies in overdensities at z > 2 (also see Elbaz et al. 2007; Tran et al. 2010). All of these observations reveal the importance of the local environment in gas accretion rate and SFR that govern the gasphase metallicity of galaxies.

Moreover, the metallicity of the infalling gas varies in different environments. In the local universe, it is observed that the metallicity of IGM gas in cosmic voids is  $<0.02\,Z_\odot$  (Stocke et al. 2007), while this number is  $\sim 0.3\,Z_\odot$  for a cluster-like environment (e.g., Mushotzky & Loewenstein 1997). This is consistent with results from the IllustrisTNG simulations (Gupta et al. 2018) that predict a metal-enhanced infalling gas in a dense environment out to  $z \sim 1.5$ . Both pieces of

evidence of lower gas accretion rate and higher metallicity of IGM gas in denser environments hint that a part of the scatter on the MZR could be due to the difference in the environment of galaxies.

The metallicity of galaxies in diverse environments is extensively studied in the local universe. Small but significant environmental dependence of the MZR is found, especially for satellite galaxies, such that at a given stellar mass, galaxies in overdensities have higher gas-phase metallicities (e.g., Cooper et al. 2008; Ellison et al. 2009; Peng & Maiolino 2014; Wu et al. 2017; Schaefer et al. 2019). Cooper et al. (2008) found that  $\gtrsim 15\%$  of the measured scatter in the MZR is caused by environmental effects. Furthermore, Peng & Maiolino (2014) found that galaxies with high metallicities favor denser environments at  $z \sim 0$ . They conclude that higher metallicity of infalling gas in dense environments is responsible for the environmental dependence of the MZR.

Beyond the local universe (at  $z\gtrsim 1$ ), the situation is unclear. Some studies found evidence of enhanced gas-phase metallicity in low-mass cluster galaxies at  $z\gtrsim 1.5$  (e.g., Kulas et al. 2013; Shimakawa et al. 2015; Maier et al. 2019). Kulas et al. (2013) used Keck/MOSFIRE observations to compare the gas-phase metallicity of 23 protocluster members ( $z\sim 2.3$ ) with 20 field galaxies. They found that the mean metallicity of low-mass galaxies ( $M_*\sim 10^{10}\,M_\odot$ ) in the protocluster is  $\sim 0.15$  dex higher than that in the field. On the other hand, Valentino et al. (2015) reported 0.25 dex lower gas-phase metallicity for the members of a  $z\sim 2$  protocluster ( $M_*\sim 10^{10.5}\,M_\odot$ ) compared to field galaxies at the same redshift. Conversely, some other studies have not observed significant environmental dependence of the MZR at high redshift (e.g., Kacprzak et al. 2015; Tran et al. 2015; Namiki et al. 2019).

With the wealth of near-IR spectroscopy for the star-forming galaxies  $(1.37 \le z \le 2.61)$  in the MOSFIRE Deep Evolution Field (MOSDEF) survey (Kriek et al. 2015), combined with the local environment measurements (Chartab et al. 2020) derived from accurate and uniformly calculated photometric redshifts with well-calibrated probability distributions, in this paper we investigate the effect of the local environment on the gas-phase metallicity of galaxies at  $z \sim 1.5$  and  $z \sim 2.3$ . In Section 2, we present the details of the MOSDEF sample used in this work. We then briefly describe the local number density measurements, as a proxy for the environment, based on the photometric observations of the CANDELS fields. We describe sample selection procedure in Section 3. In Section 4, we investigate the role of the environment in the MZR, followed by the physical interpretation of our observations. We discuss our results in Section 5 and summarize them in Section 6.

Throughout this work, we assume a flat  $\Lambda \text{CDM}$  cosmology with  $H_0 = 100 h \, \text{km s}^{-1} \, \text{Mpc}^{-1}$ ,  $\Omega_{m_0} = 0.3$ , and  $\Omega_{\Lambda_0} = 0.7$ . All magnitudes are expressed in the AB system, and the physical parameters are measured assuming a Chabrier (2003) initial mass function.

### 2. Data

### 2.1. The MOSDEF Survey

MOSDEF is an extensive near-IR spectroscopic survey conducted over 48.5 nights using the Keck/MOSFIRE spectrograph (McLean et al. 2012). As a part of the survey,  $\sim$ 1500 galaxies in five CANDELS fields (EGS, COSMOS, GOODS-N, UDS, and GOODS-S) were observed in three

redshift ranges where strong rest-optical emission lines fall within windows of atmospheric transmission (400 galaxies at  $z \sim 1.5$ , 750 at  $z \sim 2.3$ , and 400 at  $z \sim 3.4$ ). These galaxies are selected from the 3D-HST photometric and spectroscopic catalogs (Skelton et al. 2014; Momcheva et al. 2016) to a limiting Hubble Space Telescope (HST) F160W magnitude of 24.0, 24.5, and 25.0 at  $z \sim 1.5$ , 2.3, and 3.4, respectively. Based on these magnitude limits, the MOSDEF sample is roughly mass-complete down to  $M_* \sim 10^{9.5} \, M_{\odot}$  (Shivaei et al. 2015). For a full description of the survey strategy, observations, and data reduction, we refer readers to Kriek et al. (2015).

The spectral energy distributions (SED) of MOSDEF galaxies are fitted using the multiwavelength photometric data from the 3D-HST survey (Skelton et al. 2014; Momcheva et al. 2016). Briefly, the photometric fluxes are corrected for contamination caused by strong nebular emission lines measured from the MOSDEF rest-frame optical spectra. The flexible stellar population synthesis model of Conroy et al. (2009) is adopted to build a library of synthetic SEDs. Star formation histories are modeled with a delayed exponentially declining function (SFR  $\propto te^{-t/\tau}$ ), where t is the age of a galaxy and  $\tau$  is the star formation timescale. Dust attenuation is applied using the Calzetti et al. (2000) law and solar metallicity is assumed for all galaxies. Then, the SED fitting is performed using the FAST code (Kriek et al. 2009), which uses a  $\chi^2$ minimization method to find the best-fit stellar population model and corresponding properties such as stellar mass and SFR. Corresponding confidence intervals are computed by perturbing the photometry using the photometric errors. Redshifts are fixed to their spectroscopic values for the SED fitting. The spectroscopic redshifts and emission line fluxes are measured from the extracted 1D spectra, presented in Kriek et al. (2015).

### 2.2. Measuring Local Environment of Galaxies

To quantify the environment of MOSDEF galaxies, we utilize the publicly available catalog of Chartab et al. (2020), which includes measurements of local density for galaxies brighter than HST/F160W  $\leq$  26 AB mag in all of the five CANDELS fields: GOODS-S (Guo et al. 2013), GOODS-N (Barro et al. 2019), COSMOS (Nayyeri et al. 2017), EGS (Stefanon et al. 2017), and UDS (Galametz et al. 2013).

As described in Chartab et al. (2020), including both the spectroscopic and photometric redshifts for density measurements can bias the estimates in favor of galaxies with spectroscopic redshifts. Therefore, despite the availability of spectroscopic redshifts for  $\sim\!12\%$  of galaxies in the CANDELS fields, the environment catalog relies on uniformly calculated photometric redshifts (normalized median absolute deviation  $\sigma_{\rm NMAD} \sim 0.02$ ), with well-calibrated redshift probability distribution functions (PDF; Kodra 2019, D. Kodra et al. 2021, in preparation). The environment catalog has been constructed using the full photometric redshift PDFs adopting the technique of boundary-corrected, weighted von Mises kernel density estimation (Chartab et al. 2020). Here, we provide a brief explanation of density measurements.

Taking advantage of the well-calibrated and tested photometric redshift PDFs of CANDELS galaxies, the positions of galaxies are treated in a probabilistic way, such that all of the information regarding the position of a galaxy in redshift space is embedded in its photometric redshift PDF. The data set within the CANDELS fields is sliced to constant comoving

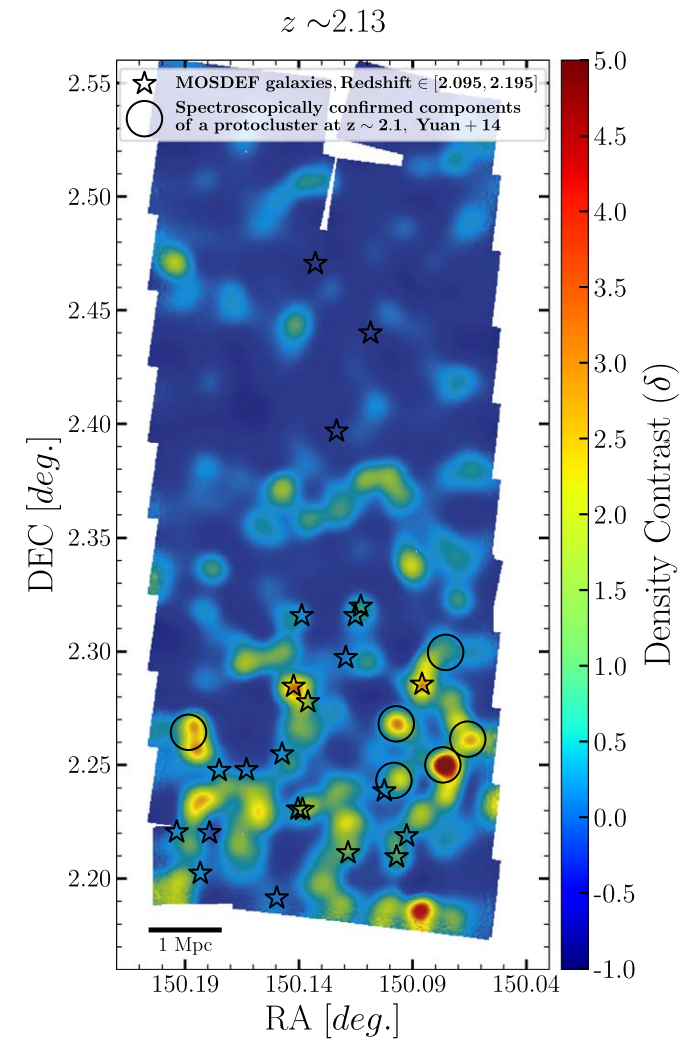


**Figure 1.** An example of the density map for the CANDELS-COSMOS field at  $z \sim 2.13$  (Chartab et al. 2020). Stars show MOSDEF sources located in this *z*-slice. Yuan et al. (2014) spectroscopically confirmed six overdensities at this redshift which were initially identified by Spitler et al. (2012). They are denoted by open circles.

width,  $\Delta\chi=35h^{-1}$  Mpc (e.g.,  $\Delta z=0.035$  at  $z\sim2$ ), which is greater than both redshift space distortion (Fingers-of-God effect; Jackson 1972) and the photometric redshift PDF resolution over the redshift range  $0.4\leqslant z\leqslant5$ . Each galaxy is distributed over all redshift slices (z-slice) based on its photometric redshift PDF, such that the galaxy has a specific weight in each z-slice. Then, to calculate the local density in each z-slice, the weighted von Mises kernel density estimation is employed. The von Mises kernel is the spherical analog of the Gaussian kernel where variables are angles (e.g., R.A. and decl.) instead of linear data (García-Portugués et al. 2013). To quantify the environment, density contrast  $(\delta)$  is defined as

$$\delta = \frac{\Sigma}{\bar{\Sigma}} - 1,\tag{1}$$

where  $\Sigma$  is the number density of galaxies at the desired point and  $\bar{\Sigma}$  is the average density in the corresponding z-slice. Figure 1 shows an example of the density map for one of the z-slices at  $z \sim 2.13$  in the COSMOS field. One should note that the probabilistic nature of the method allows us to take into account the contribution of all galaxies (based on their

photometric redshift PDFs) when we create density maps. In Figure 1 we also include six spectroscopically confirmed overdensities at  $z \sim 2.1$  (Yuan et al. 2014), which were initially discovered from the Magellan/FOURSTAR Galaxy Evolution survey (ZFOURGE; Spitler et al. 2012). We find that all six confirmed overdensities in Yuan et al. (2014) are correctly predicted in the density map.

To assign a density contrast for each galaxy, the weighted integration of the local densities over z-slices has been performed, since a galaxy with a photometric redshift is not localized in redshift space but is distributed over all z-slices based on its PDF. The densities are also corrected for a systematic underestimation near the edge of the survey footprint using the re-normalization technique.

In the following section, we cross-match the MOSDEF galaxies with the CANDELS photometric catalogs to find their associated local density measurements. Although we have spectroscopic redshifts for the MOSDEF galaxies, we do not pin them in density maps based on spectroscopic redshifts to measure their environments. The density measurements trace the relative position of galaxies in the survey and are not sensitive to systematic biases that may exist in the photometric redshifts, whereas measuring densities based on the photometric redshifts but defining positions of the MOSDEF galaxies in density maps by their spectroscopic redshifts leads to inconsistencies.

### 3. Sample Selection

We select MOSDEF galaxies that have  $H\alpha$  line luminosities with a signal-to-noise ratio  $(S/N) \ge 3$ . We only include the star-forming galaxies based on the UVJ rest-frame color selection (Muzzin et al. 2013) derived from SED fitting. Objects that are flagged as an active galactic nucleus (AGN) in the MOSDEF catalog are excluded. The AGNs are identified based on X-ray emission or IRAC colors. We also require that  $\log([\text{N II}]/\text{H}\alpha) < -0.3$  to exclude optical AGNs (Coil et al. 2015; Azadi et al. 2017, 2018; Leung et al. 2017, 2019). To have a mass-complete sample, we only consider galaxies with  $M_* \geqslant 10^{9.5} M_{\odot}$ . These criteria result in a total of 560 galaxies at  $0.78 \le z \le 2.64$ . We then cross-match these objects with the local environment catalog of Chartab et al. (2020) within a radius equal to the FWHM size of HST/F160w band pointspread function,  $\sim 0.2$ . For 23 galaxies, we could not find a source within the radius of  $\sim 0.72$  in the CANDELS photometry catalogs due to the difference in the source identification and photometry extraction between the CANDELS and the 3D-HST. Also, 15 galaxies were not included in the environment catalog since the catalog is constructed based on specific selection criteria. Each object must have (1) an SExtractor stellarity parameter < 0.95, (2) 95% of the photometric redshift PDF fall within the redshift range of  $0.4 \le z \le 5$ , and (3) an AB magnitude brighter than 26 in HST/F160W band. Fourteen out of 15 missing galaxies in the environment catalog were incorrectly identified as low-z galaxies or had very broad photometric redshift PDFs that have not satisfied the second criterion, and the other missing galaxy was identified as a galaxy with HST/F160W > 26 AB mag in the CANDELS photometric catalogs that has not satisfied the third criterion.

Figure 2 shows the comparison between the spectroscopic and the CANDELS photometric redshifts of the sample. The photometric redshift is defined as a probability-weighted

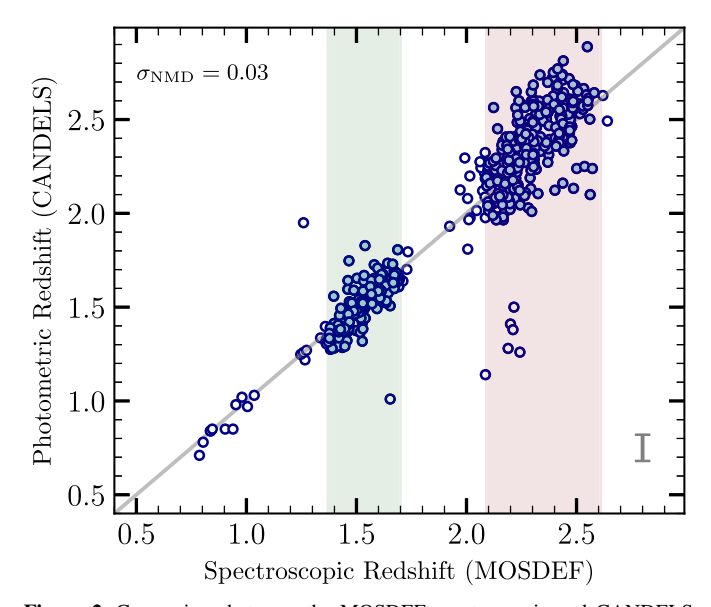


**Figure 2.** Comparison between the MOSDEF spectroscopic and CANDELS photometric redshifts of the sample. The photometric redshift is defined as a probability-weighted expectation value of the redshift based on the photometric redshift PDF. The average uncertainty on photometric redshifts is displayed in the lower right corner. The normalized median absolute deviation of the redshift for the sample is 0.03. Solid blue circles show the final sample used in this work. The green shaded region corresponds to the lower redshift bin at  $z \sim 1.5$ , and the pink region shows the highest redshift bin at  $z \sim 2.3$ . Open circles are either outliers or galaxies outside the desired redshift ranges.

expectation value of the redshift based on the photometric redshift PDF (Kodra 2019). We find a value of 0.03 for the normalized median absolute deviation of photometric redshifts. This revalidates the accuracy of photometric redshifts, which results in reliable local density measurements. Furthermore, we have removed outlier galaxies with the error >0.5 in their photometric redshifts and galaxies out of the desired redshift range (shown with open circles in Figure 2). The final sample is divided into two redshift bins, 167 galaxies at  $1.37 \leqslant z \leqslant 1.70$  and 303 galaxies  $2.09 \leqslant z \leqslant 2.61$ .

To investigate if our sample is representative of the full dynamic range of the local environment in the CANDELS data, we compare the local environmental density of CANDELS star-forming galaxies with  $M_* \ge 10^{9.5} M_{\odot}$  at the same redshift range with our sample (the MOSDEF galaxies). We use restframe UVJ colors computed in Chartab et al. (2020) to select a star-forming subsample of CANDELS galaxies. Figure 3 shows the histogram of density contrast for MOSDEF galaxies and for all of the star-forming CANDELS galaxies at the same redshift ranges. We find that MOSDEF galaxies cover a wide range of environments, making them unique for studying the environmental dependence of spectroscopic properties of galaxies. There is slight evidence that MOSDEF galaxies reside in relatively denser environments than the CANDELS star-forming sample, which is expected for most spectroscopic surveys, as they usually maximize the number of sources per mask. However, this effect is minimal in MOSDEF since it is an extensive program that covers  $\sim 600$  arcmin<sup>2</sup> at  $z \sim 2.3$  and  $\sim$ 300 arcmin<sup>2</sup> at  $z \sim 1.5$  (Kriek et al. 2015). Given the total area of the CANDELS fields (~960 arcmin<sup>2</sup>), MOSDEF covers  $\sim 30\%$  and  $\sim 60\%$  of the CANDELS area at  $z \sim 1.5$ and  $z \sim 2.3$ , respectively. This wide areal coverage translates to diverse environments in our sample, as shown in Figure 3.

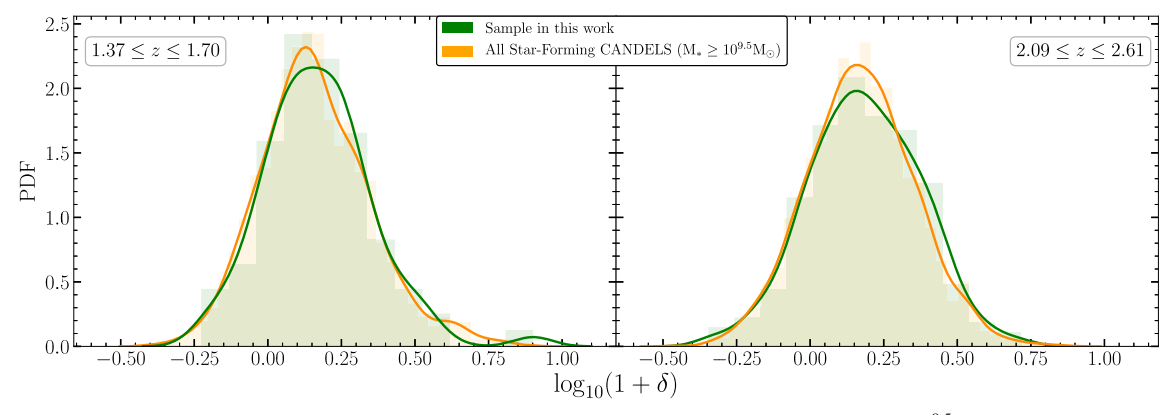


Figure 3. Histograms of overdensity measurements  $(1 + \delta)$  for all of the star-forming CANDELS galaxies with  $M_* \ge 10^{9.5} M_{\odot}$  and the sample used in this work at redshifts  $z \sim 1.5$  (left) and  $z \sim 2.3$  (right). Our sample covers a wide range of environments, making it unique to study the environmental dependence of spectroscopic properties of galaxies.

We divide the sample into three bins of environment. Although we find that the local environment distribution of our sample is well representative of the full CANDELS galaxies, we do not set the environment binning thresholds based on our sample. Instead, we calculate them from all of the star-forming CANDELS galaxies at desired redshift ranges. We find the tertiles which divide the CANDELS sample into three bins of environments, each containing a third of the sample. We consider galaxies in the lowest tertile ( $\delta < \delta_{1}$ ) as field galaxies, those within the second tertile  $(\delta_{\frac{1}{2}} \leqslant \delta < \delta_{\frac{2}{3}})$  as intermediate densities, and those in the highest tertile  $(\delta \geqslant \delta_{\frac{3}{2}})$  as overdensities. Table 1 shows the density contrast thresholds to define the field, intermediate, and overdense samples along with the sample size and the average density contrast,  $\langle 1 + \delta \rangle$  at each redshift bin. Our sample includes  $\sim$ 55 and  $\sim$ 100 galaxies in each bin of the environment at  $z \sim 1.5$  and  $z \sim 2.3$ , respectively (see Table 1).

Fossati et al. (2015) linked the observational local number density of galaxies to their parent halo masses using a stellar mass-limited sample of galaxies  $(M_* > 10^{9.5} M_{\odot})$  in semianalytic models of galaxy formation. We estimate an average halo mass  $M_{\rm halo} \gtrsim 10^{13} M_{\odot}$  for overdensities (the highest tertile in present work) at  $z \sim 2$  (also see Fossati et al. 2017). Presentday descendants of these overdensities have  $M_{\rm halo} \gtrsim 10^{14} M_{\odot}$ (Behroozi et al. 2013) and are associated with rich clusters. Massive core halos of these present-day rich cluster progenitors at  $z \sim 2$  (protoclusters) have virial radii of  $\lesssim 1$  comoving Mpc (Chiang et al. 2017), which can be observed within the CANDELS fields. Thus, our last environment bin, so-called overdensity, traces these massive cores of protoclusters at high redshift that will grow into z = 0 clusters. However, all of the dark matter and baryons that will assemble into a z = 0 cluster may be very extended at  $z \sim 2$ ,  $\sim 50$  comoving Mpc (Muldrew et al. 2015), which cannot be captured in small CANDELS fields.

We also estimate an average halo mass  $M_{\rm halo} \lesssim 10^{12.5}\,M_{\odot}$  (Fossati et al. 2015) for the lowest tertile of the environment bins, so-called field galaxies. These halos will grow into halos with  $M_{\rm halo} \lesssim 10^{13}\,M_{\odot}$  at z=0 (Behroozi et al. 2013). Thus, field galaxies in the present work are the progenitor of galaxies residing in very poor z=0 groups/clusters (like the Local Group).

In the following section, we model the MZR for our environment-selected samples to understand how metal

 Table 1

 Properties of Environment-selected Sample

Environment	Sample Size	$1 + \delta$	$\langle 1 + \delta \rangle$
	$z \sim 1.5$		
Field	53	<1.19	0.97
Intermediate density	54	1.19-1.69	1.43
Overdense	60	>1.69	2.43
	$z\sim 2.3$		
Field	97	<1.24	0.97
Intermediate density	96	1.24-1.77	1.49
Overdense	110	>1.77	2.48

enrichment processes of galaxies change with their respective environments.

### 4. Results

### 4.1. The MZR in Diverse Environments

Here we use H $\alpha$  and [N II]  $\lambda6584$  lines to estimate oxygen abundances of galaxies as an indicator for their gas-phase metallicities. However, the [N II]  $\lambda6584$  emission line is not detected at S/N  $\geqslant$  3 for 48 out of 167 and 118 out of 303 galaxies at  $z \sim 1.5$  and  $z \sim 2.3$ , respectively. As we discuss later in Appendix, requiring an [N II]  $\lambda6584$  detection biases our sample toward higher gas-phase metallicities. Therefore, to include [N II]  $\lambda6584$  nondetected galaxies in metallicity measurements, we create composite spectra by stacking the spectra of galaxies in bins of stellar mass and environment.

Following Shivaei et al. (2018), we shift individual spectra to the rest frame and then normalize them by the  $H\alpha$  luminosity. Composite spectra are computed by averaging the normalized spectra in bins of 0.5 Å considering the weights of  $1/\sigma_i^2$ , where  $\sigma_i$  is the standard deviation of the *i*th spectra. The uncertainty in the weighted average is also obtained using  $\left(\sum \frac{1}{\sigma_i^2}\right)^{-\frac{1}{2}}$ .

The resultant composite spectra are normalized to the  $H\alpha$ 

The resultant composite spectra are normalized to the  $H\alpha$  luminosity. Therefore, the average flux ratio of  $\langle \frac{[N \text{ II}]\lambda 6584}{H\alpha} \rangle$  is determined by fitting a triple Gaussian function for [N II]  $\lambda 6548,6584$  and  $H\alpha$  lines and extracting the area underneath the Gaussian function for the normalized [N II]  $\lambda 6584$  line. We

Table 2
Best-fit Linear Parameters for MZR<sup>a</sup>

Environment	α	β
	$z \sim 1.5$	
Field	$0.21 \pm 0.04$	$6.29 \pm 0.43$
Intermediate density	$0.29 \pm 0.03$	$5.51 \pm 0.31$
Overdense	$0.23\pm0.03$	$6.11 \pm 0.31$
	$z \sim 2.3$	
Field	$0.35 \pm 0.05$	$4.84 \pm 0.48$
Intermediate density	$0.31 \pm 0.04$	$5.19 \pm 0.44$
Overdense	$0.30 \pm 0.04$	$5.33 \pm 0.49$
Sanders+18 <sup>b</sup>	0.34	5.01

#### Notes.

perturb the composite spectra using their error distributions and estimate the average flux ratio for 500 trials. Also, galaxies in each bin of stellar mass and environment are bootstrap resampled in each trial to account for sample variance. The average and standard deviation of 500 trials are adopted as the flux ratio and its uncertainty.

We determine oxygen abundances (12 + log(O/H)) for the composite spectra using the Pettini & Pagel (2004) calibration of the N2 =  $\frac{[N \text{ II}]\lambda 6584}{V}$  line ratio,

$$12 + \log(O/H) = 8.9 + 0.57 \log(N2). \tag{2}$$

The intrinsic uncertainty ( $1\sigma$  dispersion) of the oxygen abundance of an individual galaxy in the calibration is 0.18. A composite spectrum consists of N galaxies; therefore, the intrinsic error in the oxygen abundance of the composite spectrum is  $0.18/\sqrt{N}$  (Erb et al. 2006; Sanders et al. 2015). To include the N2 calibration error in measurements, one can calculate the total variance of metallicity by adding the intrinsic variance to the weighted average variance from the stacks. We do not include calibration error when reporting the uncertainty in metallicities. Moreover, the N2 estimator is calibrated locally and there is some debate within the literature regarding the validity of the calibration for high-redshift galaxies (Kewley et al. 2013; Steidel et al. 2014; Shapley et al. 2019; Sanders et al. 2020). However, it does not cause a problem for our work, where we study the relative metallicities to understand the effect of the local environment on the metal content of galaxies.

We further separate our sample in different environments into three bins of stellar mass such that each bin includes an approximately equal number of galaxies. We then calculate composite line luminosities for these nine bins of environments and stellar masses and calculate composite metallicities. To determine the average MZR for each environment (field, intermediate density, and overdense), we fit a linear function to the composite metallicities and average stellar masses.

$$12 + \log(O/H) = \beta + \alpha \log\left(\frac{M_*}{M_\odot}\right), \tag{3}$$

where  $\alpha$  and  $\beta$  are the slope and intercept of the linear function, respectively. The best-fit parameters and errors are given in

Table 2. To estimate errors, we perturb metallicities according to their uncertainties and repeat the fitting process 500 times. We also include best-fit parameters from Sanders et al. (2018) for the MOSDEF galaxies at  $z \sim 2.3$ . Their sample is the same as ours except that they have one more constraint on the detection (S/N > 3) of the  $H\beta$  emission line.

The resulting MZRs in different environments are shown in Figure 4 along with the metallicity and stellar mass of individual galaxies. The metallicity measurements for the composite spectra are shown with diamonds. We find an enhancement in the gas-phase metallicity of galaxies in dense environments at  $z \sim 1.5$  compared to the field galaxies, while the trend reverses at  $z \sim 2.3$  such that galaxies in the dense environment tend to have lower metallicities compared to their counterparts in lower-density environments.

At  $z \sim 1.5$ , the average galaxies with  $10^{9.5} M_{\odot} \lesssim M_* \lesssim 10^{11} M_{\odot}$  that reside in overdensities have enhanced metallicities by  $\sim 0.07$  dex compared to their field counterparts. At the low stellar mass end of the MZR, this enhancement is less significant, mostly due to a higher fraction of [N II]  $\lambda 6584$  nondetection galaxies in the low-mass end. At  $z \sim 2.3$ , the average galaxies with  $10^{9.5} M_{\odot} \lesssim M_* \lesssim 10^{11} M_{\odot}$  in the dense environment are  $\sim 0.11$  dex metal deficient relative to the field galaxies at the same stellar mass range.

A notable caveat for studies with a small sample size, which is the case for most of the high-redshift spectroscopic samples, is the presence of dissimilar stellar mass distributions among the galaxies in different environments. It is crucial to have the same stellar mass distributions in different environments to properly study the effect of the environment on the gas-phase metallicity of galaxies at a given stellar mass. As we bin the data to find the average MZR in diverse environments, different stellar mass distributions can result in different average metallicities. This difference can be misinterpreted as an environmental imprint on the MZR. Therefore, before proceeding to a discussion of our results, in the next section, we first perform an analysis on a mass-controlled sample of galaxies where we carefully match the stellar mass distribution of galaxies in different environments and find the composite spectra for the mass-controlled sample. This allows us to properly disentangle the effect of stellar mass from that of the local environment, providing an unbiased measurement of environmental trend.

### 4.2. Mass-controlled Sample

The stellar mass distribution of our sample is shown in Figure 5. As expected, galaxies in diverse environments have different stellar mass distributions. We find that overdensities tend to have a higher fraction of massive galaxies compared to underdense regions. For instance, the median stellar mass of our field sample at  $z \sim 1.5$  is  $10^{9.9} M_{\odot}$ , while this value for the overdense sample is  $10^{10.25} M_{\odot}$ . In the highest redshift bin,  $z \sim 2.3$ , the median stellar masses are  $10^{9.93} M_{\odot}$  and  $10^{10.17} M_{\odot}$  for field and overdense galaxies, respectively. It is, therefore, important to match the stellar mass distribution of galaxies in different environments to properly disentangle the effect of the local environment on the gas-phase metallicity from that of the stellar mass. As shown in Figure 5, we match the stellar mass distribution of galaxies in three environment bins by subsampling the galaxies such that each environment has the same number of galaxies at a given stellar mass. We adopt a resolution of  $\log(M_*/M_{\odot}) = 0.1$  dex when matching the stellar

<sup>&</sup>lt;sup>a</sup> Best-fit parameters for  $12 + \log(O/H) = \beta + \alpha \log(M_*/M_{\odot})$ .

<sup>&</sup>lt;sup>b</sup> Best-fit parameters from Sanders et al. (2018) for MOSDEF galaxies at  $z \sim 2.3$  without any constraint on their environments.

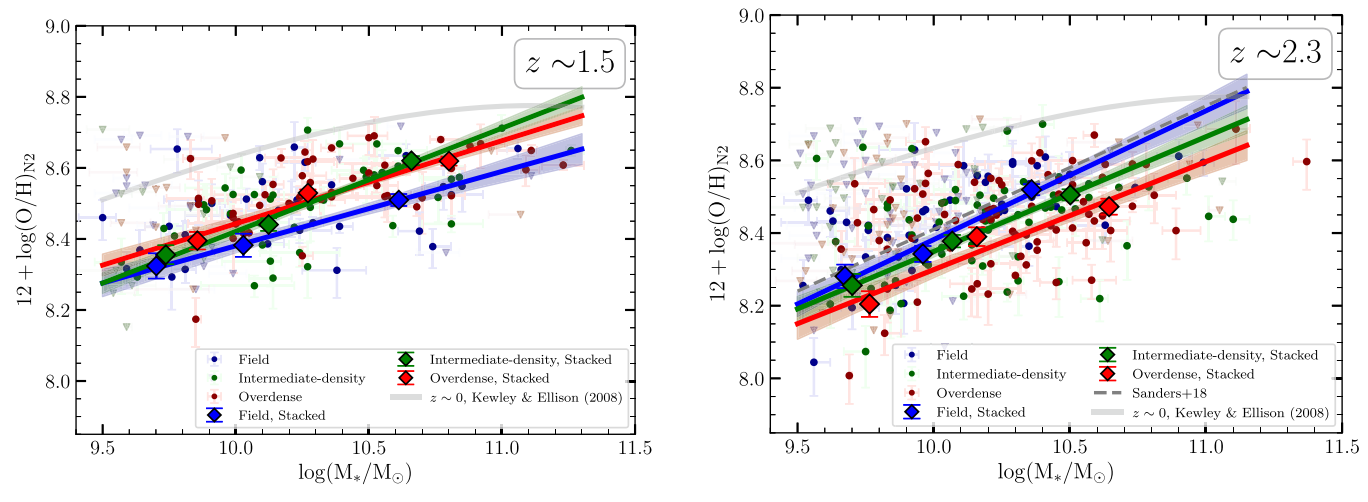


Figure 4. MZR at  $z \sim 1.5$  (left) and at  $z \sim 2.3$  (right) for galaxies residing in three different environments: overdensity (red), intermediate density (green), and underdensity (blue). For [N II]  $\lambda$ 6584 nondetections, the upper limit of the metallicity is shown with inverted triangle symbols. The metallicity measurements for the composite spectra are shown with diamonds. The fitted average MZR lines (based on Table 2) for different environments are shown along with the  $1\sigma$  error bars (the shaded regions around the best-fit models). The best-fit models suggest that the metallicity at a given stellar mass enhances in denser environments at  $z \sim 1.5$ , while the trend reverses at  $z \sim 2.3$  such that galaxies in denser environments tend to have lower metallicities. Errors in the metallicities of composite spectra are not shown as they are smaller than the symbols (diamond). The Sloan Digital Sky Survey local MZR (Kewley & Ellison 2008) is shown by a solid gray line and the average MZR for all the MOSDEF galaxies at  $z \sim 2.3$  from Sanders et al. (2018) is indicated by a dashed gray line.

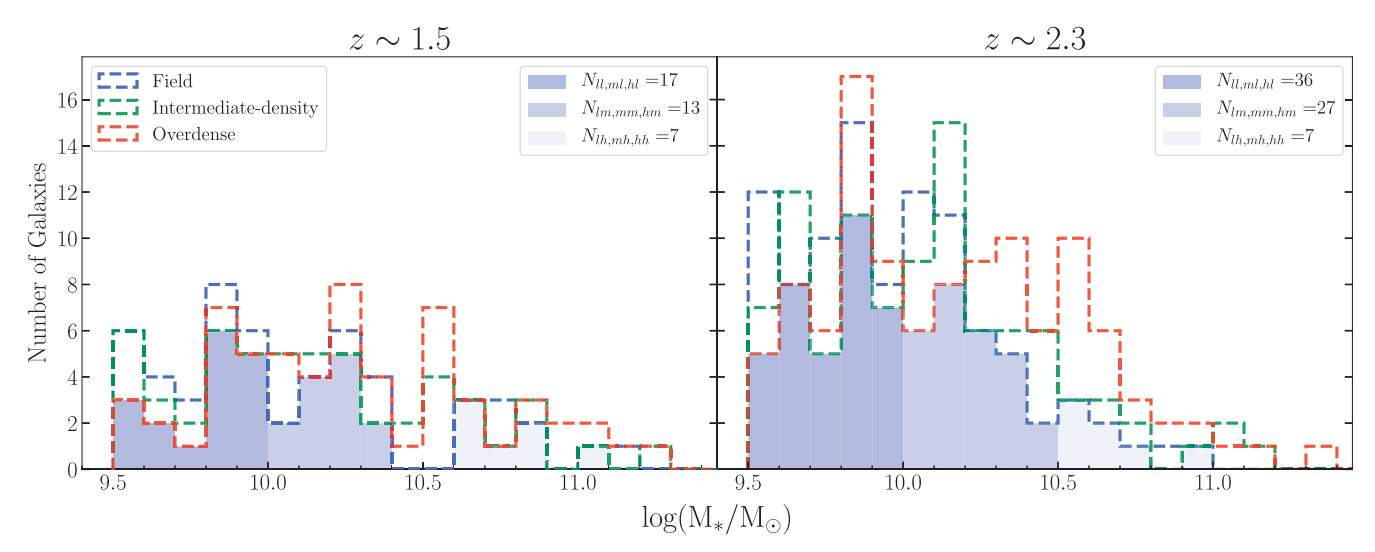


Figure 5. Histograms of stellar mass for the sample in different environments (dashed lines). Shaded regions show subsampled data with the matched stellar mass distributions. At a given stellar mass, subsampled data have the same number of galaxies in every environment bin. The number of galaxies in each subsampled bin is shown in the format of  $N_{xy}$ , where x shows the type of environment and y shows the stellar mass range ("t": low, "t": intermediate, and "t": high). For example,  $N_{th} = 7$  at t at t

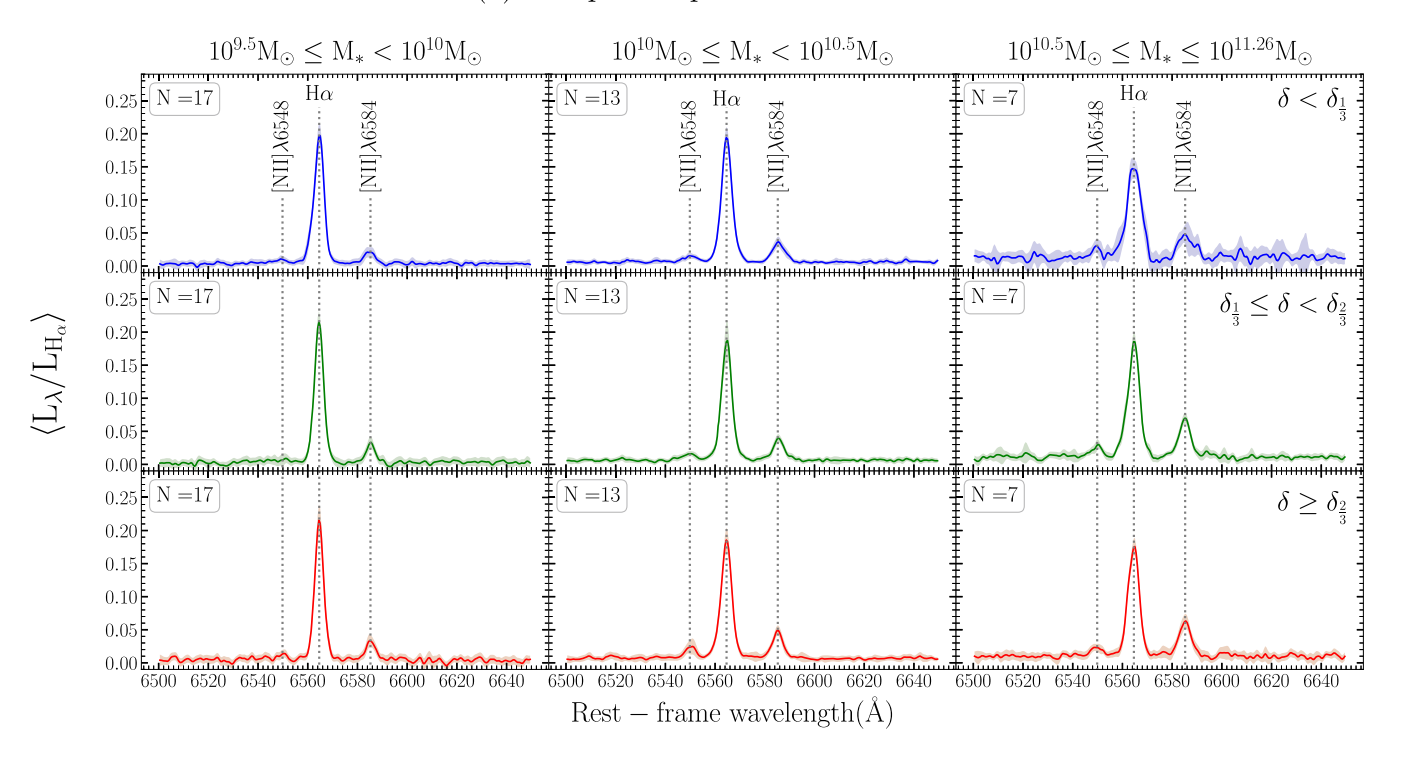
mass distributions. In other words, we draw a fraction of galaxies in different environments such that they have the same stellar mass distributions with 0.1 dex resolution. As there are not unique mass-matched subsamples in different environments, we repeat subsampling 500 times. For each trial, we measure the composite spectra in the bins of environment and stellar mass using the same procedure described in Section 4.1. The stellar mass bins of  $9.5 \leqslant \log(M_*/M_\odot) < 10$ ,  $10 \leqslant \log(M_*/M_\odot) < 10.5$ , and  $\log(M_*/M_\odot) \geqslant 10.5$  are adopted. We perturb the resultant composite spectra of each trial according to their uncertainties. Ultimately, we construct the final mass-controlled composite spectra and their errors, using the average and standard deviation of the 500 measurements, respectively.

We do not take into account stellar mass uncertainties when matching the stellar mass distribution of galaxies in different environments, since the median uncertainty of stellar masses in our sample is  $\sim\!0.05$  dex, which is smaller than the desired resolution in the mass-controlled sample, 0.1 dex.

### 4.2.1. Metallicity of Mass-controlled Sample

The composite spectra for the nine bins of stellar masses and environments for the mass-controlled sample are shown in Figure 6. The  $\frac{[N \text{ II}]\lambda 6584}{H\alpha}$  estimates and gas-phase metallicity (oxygen abundance) for mass-controlled composite spectra in the nine bins of stellar masses and environments are presented

### (a) Composite spectra: $z \sim 1.5$



## (b) Composite spectra: $z \sim 2.3$

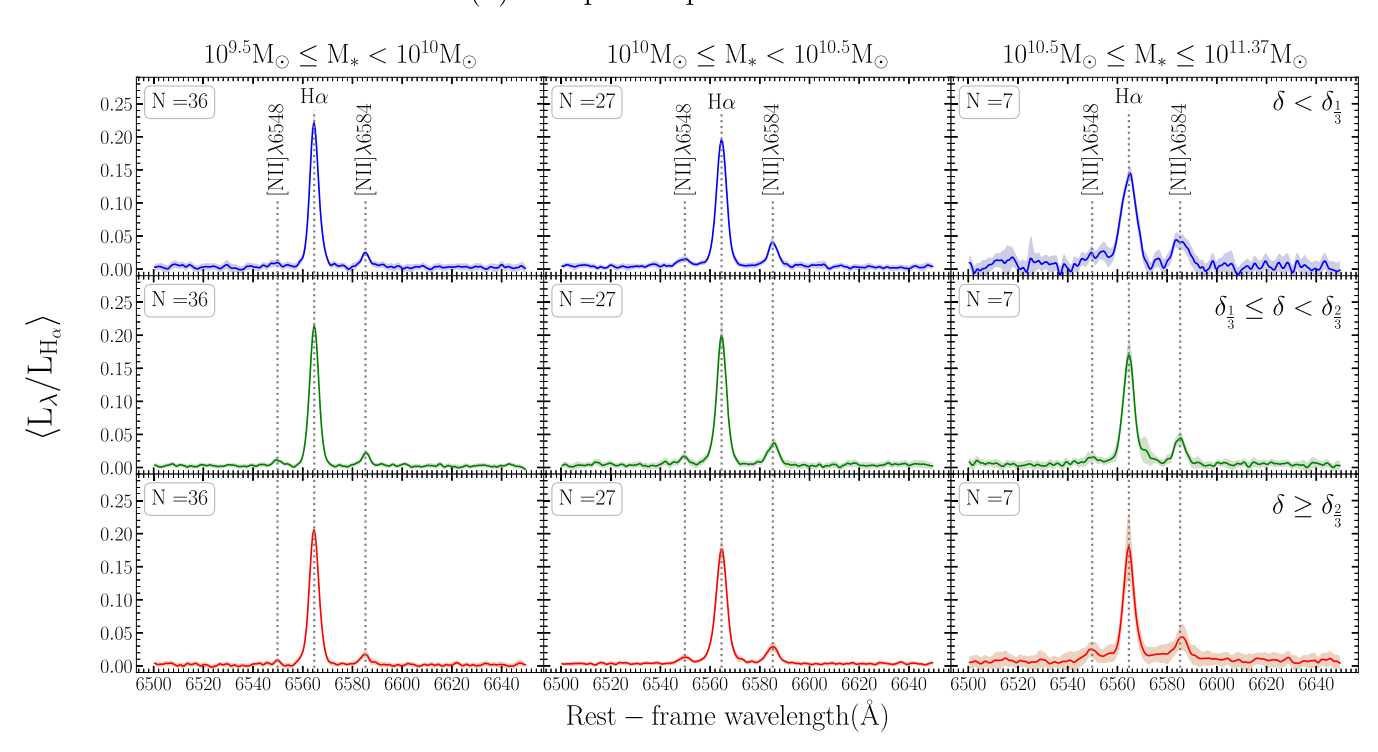


Figure 6. Composite spectra for the mass-controlled samples in the bins of stellar mass and environment at  $z \sim 1.5$  (top) and  $z \sim 2.3$  (bottom). Errors are represented with the shaded regions, which are around the weighted average spectra. To build the composite spectra for the mass-controlled samples, we use the subsampling technique. Every time we subsample the data such that they have similar stellar mass distributions in three bins of environment, we build the composite spectra and perturb them according to their uncertainties. In the end, using the average and standard deviation of 500 trials, we construct mass-controlled composite spectra and their errors, respectively.

 Table 3

 Properties of the Composite Spectra for the Mass-controlled Sample

Environment	$N_{ m T}^{ m a}$	$N^{\mathbf{b}}$	$\langle \log \frac{M_*}{M_{\odot}} \rangle$	$\langle \log(\text{SFR}[\frac{M_{\odot}}{\text{year}}]) \rangle$	$\langle N2 \rangle = \langle \frac{[N \text{ II}] \lambda 6584}{H\alpha} \rangle$	$\langle 12 + \log(O/H) \rangle$
Field	27	17	$9.79 \pm 0.03$	$0.89 \pm 0.24$	$0.090 \pm 0.015$	$8.305 \pm 0.042$
	16	13	$10.20\pm0.03$	$1.15\pm0.23$	$0.164 \pm 0.014$	$8.452 \pm 0.022$
	9	7	$10.78\pm0.05$	$1.15\pm0.35$	$0.246 \pm 0.040$	$8.552 \pm 0.040$
Intermediate density	22	17	$9.81 \pm 0.04$	$0.75 \pm 0.18$	$0.130 \pm 0.016$	$8.395 \pm 0.030$
	21	13	$10.20 \pm 0.03$	$1.08\pm0.32$	$0.169 \pm 0.013$	$8.459 \pm 0.019$
	7	7	$10.75\pm0.05$	$1.31\pm0.36$	$0.335 \pm 0.018$	$8.629 \pm 0.013$
Overdense	18	17	$9.81 \pm 0.03$	$0.78 \pm 0.20$	$0.132 \pm 0.016$	$8.400 \pm 0.030$
	17	13	$10.21 \pm 0.03$	$1.26 \pm 0.29$	$0.216 \pm 0.015$	$8.520 \pm 0.018$
	9	7	$10.79\pm0.05$	$1.44\pm0.36$	$0.303 \pm 0.022$	$8.604 \pm 0.014$
2.09–2.61 Field	53	36	$9.77 \pm 0.02$	$0.92 \pm 0.16$	$0.090 \pm 0.009$	$8.305 \pm 0.023$
	36	27	$10.22\pm0.02$	$1.27\pm0.16$	$0.180 \pm 0.011$	$8.476 \pm 0.015$
	7	7	$10.65\pm0.06$	$1.09\pm0.24$	$0.308 \pm 0.031$	$8.609 \pm 0.025$
Intermediate density	42	36	$9.76 \pm 0.02$	$0.91 \pm 0.14$	$0.084 \pm 0.008$	$8.288 \pm 0.022$
	42	27	$10.21 \pm 0.02$	$1.28 \pm 0.16$	$0.165 \pm 0.013$	$8.454 \pm 0.020$
	9	7	$10.66\pm0.02$	$1.38 \pm 0.16$	$0.219 \pm 0.020$	$8.524 \pm 0.023$
Overdense	45	36	$9.77 \pm 0.02$	$0.99 \pm 0.13$	$0.072 \pm 0.011$	$8.249 \pm 0.036$
	39	27	$10.21\pm0.02$	$1.31\pm0.14$	$0.144 \pm 0.014$	$8.420 \pm 0.024$
	21	7	$10.66\pm0.03$	$1.51\pm0.39$	$0.209 \pm 0.038$	$8.512 \pm 0.024$
	Field  Intermediate density  Overdense  Field  Intermediate density	Field 27 16 9 Intermediate density 22 21 7 Overdense 18 17 9 Field 53 36 7 Intermediate density 42 42 9 Overdense 45 39	Field 27 17 16 13 9 7  Intermediate density 22 17 21 13 7 7  Overdense 18 17 17 13 9 7  Field 53 36 36 27 7 7  Intermediate density 42 36 42 27 9 7  Overdense 45 36 39 27		Field 27 17 9.79 $\pm$ 0.03 0.89 $\pm$ 0.24 16 13 10.20 $\pm$ 0.03 1.15 $\pm$ 0.23 9 7 10.78 $\pm$ 0.05 1.15 $\pm$ 0.35 Intermediate density 22 17 9.81 $\pm$ 0.04 0.75 $\pm$ 0.18 21 13 10.20 $\pm$ 0.03 1.08 $\pm$ 0.32 7 10.75 $\pm$ 0.05 1.31 $\pm$ 0.36 Overdense 18 17 9.81 $\pm$ 0.03 0.78 $\pm$ 0.20 17 13 10.21 $\pm$ 0.03 1.26 $\pm$ 0.29 9 7 10.79 $\pm$ 0.05 1.44 $\pm$ 0.36 Field 53 36 9.77 $\pm$ 0.02 0.92 $\pm$ 0.16 36 27 10.22 $\pm$ 0.02 1.27 $\pm$ 0.16 7 7 10.65 $\pm$ 0.06 1.09 $\pm$ 0.24 Intermediate density 42 36 9.76 $\pm$ 0.02 0.91 $\pm$ 0.14 42 27 10.21 $\pm$ 0.02 1.28 $\pm$ 0.16 Overdense 45 36 9.77 $\pm$ 0.02 0.99 $\pm$ 0.13 1.31 $\pm$ 0.14	Field 27 17 9.79 $\pm$ 0.03 0.89 $\pm$ 0.24 0.090 $\pm$ 0.015 16 13 10.20 $\pm$ 0.03 1.15 $\pm$ 0.23 0.164 $\pm$ 0.014 9 7 10.78 $\pm$ 0.05 1.15 $\pm$ 0.35 0.246 $\pm$ 0.040 Intermediate density 22 17 9.81 $\pm$ 0.04 0.75 $\pm$ 0.18 0.130 $\pm$ 0.016 21 13 10.20 $\pm$ 0.03 1.08 $\pm$ 0.32 0.169 $\pm$ 0.013 7 7 10.75 $\pm$ 0.05 1.31 $\pm$ 0.36 0.335 $\pm$ 0.018 Overdense 18 17 9.81 $\pm$ 0.03 0.78 $\pm$ 0.20 0.132 $\pm$ 0.016 17 13 10.21 $\pm$ 0.03 1.26 $\pm$ 0.29 0.216 $\pm$ 0.015 9 7 10.79 $\pm$ 0.05 1.44 $\pm$ 0.36 0.303 $\pm$ 0.022 Field 53 36 9.77 $\pm$ 0.02 0.92 $\pm$ 0.16 0.180 $\pm$ 0.011 7 7 7 10.65 $\pm$ 0.06 1.09 $\pm$ 0.24 0.308 $\pm$ 0.031 Intermediate density 42 36 9.76 $\pm$ 0.02 0.91 $\pm$ 0.14 0.084 $\pm$ 0.008 42 27 10.21 $\pm$ 0.02 1.28 $\pm$ 0.16 0.165 $\pm$ 0.013 9 7 10.66 $\pm$ 0.02 1.38 $\pm$ 0.16 0.219 $\pm$ 0.020 Overdense 45 36 9.77 $\pm$ 0.02 0.99 $\pm$ 0.13 0.072 $\pm$ 0.011 39 27 10.21 $\pm$ 0.02 1.38 $\pm$ 0.16 0.219 $\pm$ 0.020 Overdense 45 36 9.77 $\pm$ 0.02 0.99 $\pm$ 0.13 0.072 $\pm$ 0.011 39 27 10.21 $\pm$ 0.02 1.38 $\pm$ 0.16 0.219 $\pm$ 0.020

#### Notes.

in Table 3. We follow the same procedure as described in Section 4.1 to measure the metallicity of galaxies in the bins of environment and stellar mass from the composite spectra using the N2 indicator.

We also measure the average stellar masses and SFRs of the mass-matched samples in stellar mass and environment bins. We use SFRs derived from SED fitting since the dust-corrected  $H\alpha$  luminosity is not available for 40% of our sample. We avoid imposing a constraint on the detection of the H $\beta$ emission line needed for dust correction, as it decreases our sample size significantly. The variation of metallicity at fixed  $M_*$  in different environments is small (<0.1 dex) and thus requires large sample sizes to be detected. Previous studies found that the SED-derived SFRs for MOSDEF galaxies are in general agreement with SFRs derived from dust-corrected H $\alpha$ luminosities (Reddy et al. 2015; Shivaei et al. 2016). The average SED-derived SFRs listed in Table 3 suggest that even though there is evidence for a weak environmental dependence of the SFRs for our star-forming sample at a given stellar mass, it is not significant due to large uncertainties in the SFR measurements. Errors of SFRs listed in Table 3 include uncertainty in the SFR of individual galaxies as well as sample variance. A detailed study of the environmental imprints on specific SFRs of MOSDEF galaxies can properly constrain this relation. Old et al. (2020) have used [OII]-derived SFRs to investigate this relation at 1.0 < z < 1.5 in Gemini Observations of Galaxies in Rich Early Environments Survey (GOGREEN; Balogh et al. 2017). They find no significant difference between the specific SFR of the cluster and the field sample

The MZR for the mass-controlled sample at  $z \sim 1.5$  and  $z \sim 2.3$  are presented in Figure 7. We emphasize that the stellar mass distributions in the environment bins are similar. This allows us to remove the effect of stellar mass on metallicity to

properly investigate the environmental effects. Also, although the mass-matched sample has a smaller number of galaxies than does the whole sample, we subsample the data 500 times to incorporate the contribution of the full sample in measurements. As shown in Figure 7, we find that at a given stellar mass, the metallicity of galaxies changes with their respective environments at both redshift intervals considered here.

At  $z\sim1.5$ , the average metallicity of galaxies in overdensities is higher than that of field galaxies, with enhancements of  $0.094\pm0.051$  ( $1.8\sigma$  significance),  $0.068\pm0.028$  ( $2.4\sigma$  significance), and  $0.052\pm0.043$  ( $1.2\sigma$  significance) dex for the mass-controlled sample with  $M_*\sim10^{9.8}\,M_\odot$ ,  $10^{10.2}\,M_\odot$ , and  $10^{10.8}\,M_\odot$ , respectively. For galaxies residing in the intermediate density, the metallicity enhancements are  $0.090\pm0.052$  ( $1.7\sigma$  significance),  $0.007\pm0.029$  (insignificant), and  $0.077\pm0.042$  ( $1.8\sigma$  significance) dex at the same stellar masses mentioned above.

In contrast, at  $z\sim2.3$ , the average metallicity of galaxies in overdensities is lower than that of their field counterparts. Galaxies in the mass-controlled sample that reside in overdensities with  $M_*\sim10^{9.8}\,M_\odot$ ,  $10^{10.2}\,M_\odot$ , and  $10^{10.7}\,M_\odot$ , are metal deficient by  $0.056\pm0.043$  ( $1.3\sigma$  significance),  $0.056\pm0.028$  ( $2\sigma$  significance), and  $0.096\pm0.034$  ( $2.8\sigma$  significance) dex relative to the field sample, respectively. At this redshift, the metal deficiencies are  $0.017\pm0.032$  (insignificant),  $0.022\pm0.025$  (insignificant), and  $0.085\pm0.034$  ( $2.5\sigma$  significance) dex for galaxies located in the intermediate density with the same stellar masses as above.

Analysis of the mass-controlled samples confirms the trends already observed for the unmatched sample in Figure 4; however, the significance of observed trends is more reliable when we control the stellar mass distribution of the sample. Considering all stellar mass ranges  $(10^{9.5}\,M_\odot \lesssim M_* \lesssim 10^{11}\,M_\odot)$ , at  $z\sim 1.5$ , on average galaxies in overdensities are  $\sim 0.07$  dex richer in metals compared to their field counterparts.

<sup>&</sup>lt;sup>a</sup> Total number of galaxies in the bins of environment and stellar mass which is subsampled 500 times.

<sup>&</sup>lt;sup>b</sup> Number of galaxies in each subsample (shaded region in Figure 5).

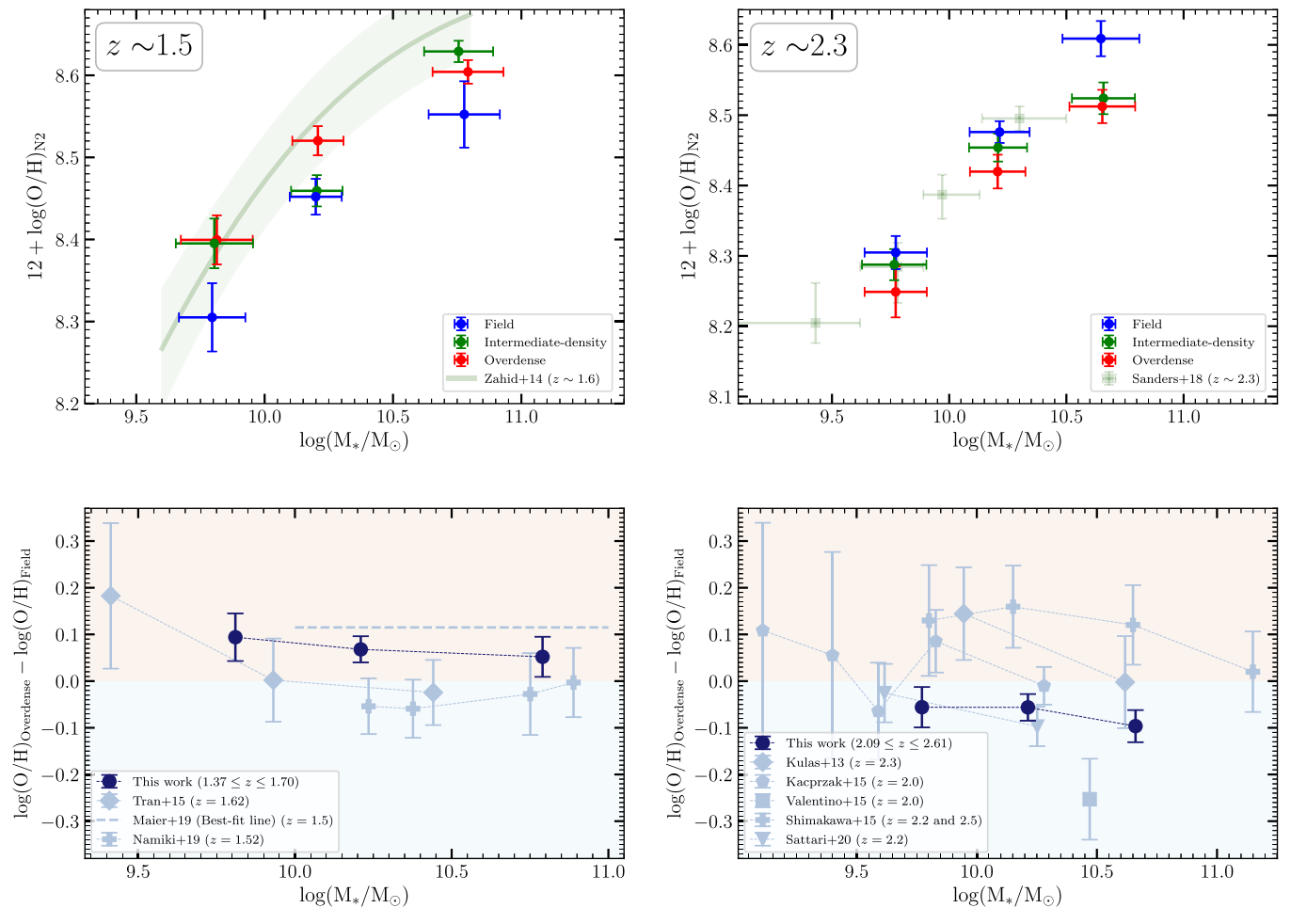


Figure 7. Top panels: MZR for mass-matched sample at  $z \sim 1.5$  (left) and  $z \sim 2.3$  (right) in three different environments: field (blue), intermediate density (green) and overdense (red). Three stellar mass bins are fixed at  $9.5 \le \log(M_*/M_\odot) < 10$ ,  $10 \le \log(M_*/M_\odot) < 10.5$  and  $\log(M_*/M_\odot) \ge 10.5$  and error bars in stellar masses show the  $1\sigma$  scatter of the data around the average value. Bottom panels: the offset between the average metallicity of galaxies in overdensities (protocluster/cluster) and that of field galaxies as a function of stellar mass at  $z \sim 1.5$  (left) and  $z \sim 2.3$  (right). For comparison, previous studies in the literature at both redshifts are also included in the panels (see Section 5.1 for details).

In contrast, at  $z\sim 2.3$ , average galaxies in overdensities have  $\sim 0.07$  dex lower metallicities compared to the field galaxies. Before discussing the physical origin of the observed trends in detail, we compare our results with previous works in the following section.

### 5. Discussion

### 5.1. Comparison with Previous Works

Only a handful of studies have been conducted to investigate the role of the environment in the MZR at z > 1. The bottom panels in Figure 7 show the offset between the average metallicity of galaxies in overdensities (protocluster/cluster) and that of field galaxies as a function of stellar mass at both redshift bins,  $z \sim 1.5$  and 2.3. In these figures, we also include the aforementioned offsets from the literature. Our finding at  $z \sim 1.5$  is in full agreement with the recent work of Maier et al. (2019). They studied a massive cluster at  $z \sim 1.5$  and found that, at a given stellar mass, the metallicities of galaxies in the inner part of the cluster are higher by  $\sim 0.1$  dex than those of infalling and field galaxies. They suggest that strangulation in the dense cores of clusters results in a cold gas removal that enhances the metallicity. However, Namiki et al. (2019) and Tran et al. (2015) found no significant environmental

dependence of the MZR around  $z \sim 1.5$ . Namiki et al. (2019) compared the MZR of narrowband H $\alpha$ -selected cluster members with the field MZR of Stott et al. (2013). Tran et al. (2015) considered the field sample of Zahid et al. (2014) for the comparison. Therefore, we also utilize the field samples of Stott et al. (2013) and Zahid et al. (2014) to measure the metallicity offset (shown in Figure 7) for the studies of Namiki et al. (2019) and Tran et al. (2015), respectively.

In the studies regarding the environmental dependence of the MZR, the sample selection bias needs to be handled properly to ensure that both field and cluster samples are selected in the same way. For example, Stott et al. (2013) found that  $H\alpha$ emitting galaxies selected from the High-Z Emission Line Survey (HiZELS; Sobral et al. 2013) have remarkably higher metallicity at a given stellar mass compared to a rest-frame UVselected sample of Erb et al. (2006). They argued that the UVselected sample of Erb et al. (2006) tends to have a higher average SFR compared to the HiZELS narrowband-selected sample, resulting in a bias against metal-rich galaxies. Therefore, the comparison between the MZR of two different works can be biased due to the selection criteria. However, this is not an issue when the sample is selected uniformly in different environments and measurements are performed consistently. Shimakawa et al. (2015) studied narrowband-selected galaxies

in two rich overdensities at z=2.2 and 2.5. They found that the metallicity of protocluster galaxies  $(M_* < 10^{11} \, M_\odot)$  is  $\sim 0.15$  dex higher than that of field galaxies, which contrasts with our result at  $z \sim 2.3$ . According to Stott et al. (2013) and discussions included in Shimakawa et al. (2015), selection bias is a potential concern in their study since different criteria are used for the selection of protocluster (narrowband selected) and field (UV selected, Erb et al. 2006) galaxies. This concern can be addressed in future studies by comparing the protocluster MZR of Shimakawa et al. (2015) with a field MZR of a narrowband-selected H $\alpha$  emitters at  $z \sim 2.2$ .

Kacprzak et al. (2015) and Alcorn et al. (2019) studied the MZR of a protocluster (Yuan et al. 2014) at z = 2.1 and reported no significant environmental effect on the MZR. As shown in Figure 1, we also captured this protocluster in the present work. We speculate that the lack of environmental dependence of the MZR in their studies can originate from the consideration of all the protocluster members at the same density contrast. As seen in Figure 1, the protocluster includes different components, and considering that all the members are located in an overdensity weakens any existing environmental dependence of the MZR.

Valentino et al. (2015) found that cluster star-forming galaxies ( $10^{10}\,M_\odot \leqslant M_* \leqslant 10^{11}\,M_\odot$ ) are  $\sim 0.25$  dex poorer in metals than their field counterparts at  $z\sim 2$ . We find a similar trend at  $z\sim 2.3$  with a lower average metal deficiency of  $\sim 0.1$  dex. Moreover, Z. Sattari et al. (2021, in preparation) studied a massive protocluster at z=2.2 (Darvish et al. 2020) and found that protocluster galaxies with  $M_*\sim 10^{9.6}\,M_\odot$  and  $M_*\sim 10^{10.2}\,M_\odot$  are  $0.03\pm 0.06$  and  $0.10\pm 0.04$  dex metal deficient, respectively, compared to field galaxies. Our findings at  $z\sim 2.3$  are in agreement with their results.

In the presence of limited sample size, an unbalanced stellar mass distribution of galaxies between cluster members and the field sample can affect the environmental trends. In other words, even in each stellar mass bin (e.g.,  $9.5 \leq \log(M_*/M_{\odot}) < 10$ ), the stacked spectra are biased toward massive galaxies, which are usually detected with higher S/N. Therefore, one needs to match the shape of stellar mass distributions in different environments as described in Section 4.2, and having the same average/median stellar mass in the bins of the environment does not guarantee that the effect of stellar mass on gas-phase metallicity is removed properly. Kulas et al. (2013) have studied the MZR of a protocluster at  $z \sim 2.3$  and reported a 0.1 dex metallicity enhancement with respect to the field galaxies. We do not confirm such trends in the present work. Their field and protocluster samples are selected consistently (UV selected). However, based on Figure 2 of Kulas et al. (2013), we speculate that the metallicity enhancement seen in their work can be affected by the significantly different stellar mass distributions of their protocluster and field samples.

Beyond the local universe, all of the previous works regarding environmental dependence of gas-phase metallicity are conducted by comparing MZR for a cluster/protocluster and a sample of field galaxies. However, within a given cluster/protocluster, galaxies may have different density contrasts. Thus, quantifying the environment using local density is a better approach to study environmental effect rather than considering all of the members of a cluster/protocluster residing in an overdensity. For instance, Maier et al. (2019) found that the metallicity enhancement at  $z \sim 1.5$ 

is only observed for the core (inside half of  $R_{200}$ ) of a cluster, not for infalling protocluster members. Assuming that all of the cluster/protocluster members have similar local densities weakens any underlying environmental dependence of the MZR. In the present work, for the first time, we study the gasphase metallicity of galaxies as a function of their local density and its evolution with cosmic time beyond the local universe. Similar works have been conducted by Mouhcine et al. (2007), Cooper et al. (2008), and Peng & Maiolino (2014) with a Sloan Digital Sky Survey sample at  $z \sim 0$ .

### 5.2. How Does the Environment Affect MZR?

In this work, we find that galaxies in overdense regions have lower metallicities than do their field counterparts at  $z \sim 2.3$ , but they become more metal rich as they evolve to  $z \sim 1.5$ . In other words, the gas-phase metallicity of galaxies in a dense environment increases by  $\sim 0.15$  dex as they evolve from  $z \sim 2.3$  to  $z \sim 1.5$  ( $\sim 1.5$  Gyr), but the metallicity of field galaxies are almost unchanged over this period. It implies that, at high redshift, metal enrichment processes are affected by the environment in which galaxies reside.

Previous studies observed that dense environments at the early stage of galaxy cluster formation  $(z \ge 2)$  contain a significant fraction of pristine gas (e.g., Cucciati et al. 2014). In the absence of gravitational heating processes, gas accretion in overdensities should be more prominent due to their deep potential well. However, infalling gas in overdensities with massive halos gets shock heated and needs to radiate its kinetic energy to accrete into the halo. At high redshifts, where the average density of the universe is higher by a factor of  $(1+z)^3$ , gas cooling is very efficient (van de Voort & Schaye 2012). It is also observed that overdense regions in the early universe are not only overdense in galaxies but also contain a large fraction of dense gas (e.g., Hennawi et al. 2015). Denser gas can cool down faster, facilitating the accretion of the metal-poor primordial gas into galaxies (Kereš et al. 2005; Dekel & Birnboim 2006). As a result, the prominent accretion of cold metal-poor gas in overdensities dilutes the metal content of ISM in galaxies at high redshifts. This results in the metal-poor gas in the galaxies residing in dense environments at high redshifts, as observed in the present work at  $z \sim 2.3$ . Valentino et al. (2015) also observed the same metal deficiency at  $z \sim 2$ and concluded that the accretion of pristine gas from clusterscale reservoirs lowers the gas-phase metallicity of galaxies in dense environments compared to their coeval field galaxies.

In contrast, at the lower redshift,  $z \lesssim 2$ , the gas cannot cool down efficiently in overdensities, so the galaxies in those regions start to experience cosmological starvation. The lack of pristine metal-poor gas accretion in cluster members has been observed in different simulations out to  $z \sim 2$  (van de Voort et al. 2017; Gupta et al. 2018). Moreover, Gupta et al. (2018) studied chemical preprocessing of cluster galaxies in the IllustrisTNG cosmological simulation and found that at z = 1.5, cluster galaxies receive ~0.05 dex more metal-rich infalling gas than galaxies in the field. But, this metallicity enhancement disappears at higher redshifts (z > 1.5). At  $z \sim 2$ , when galaxies actively form their stars, feedback processes should be strong enough to expel part of the processed gas into the IGM through the outflows. As a result, crowded regions contain preprocessed and metal-enriched gas, which can be then re-accreted to the galaxies at lower redshifts. As preprocessed gas has a higher metallicity, it can cool down faster, which facilitates its

accretion (Kereš et al. 2005; Dekel & Birnboim 2006). Therefore, we speculate that both effects, suppressed primordial metal-poor gas infall and preprocessed metal-enriched gas accretion, are essential in ramping up metal production in a dense environment around  $z\lesssim 2$ . This can explain our result at  $z\sim 1.5$ , where we find metallicity enhancement for galaxies in overdensities compared to field galaxies.

In the absence of cold gas accretion, galaxies could maintain their SFR unchanged for a period of time as they start to consume their gas reservoirs. This time ranges from a few hundred megayears for most massive galaxies up to a few gigayears for low-mass galaxies (McGee et al. 2014; Balogh et al. 2016). However, the dilution of the ISM's metal content will cease immediately after the termination of cold gas accretion. Therefore, the absence of SFR suppression in overdense regions at  $z \sim 1.5$  for our star-forming sample does not contradict the observed metal enhancement in galaxies residing in overdensities at that redshift. Given the relatively short cosmic time interval between  $z \sim 2.3$  and  $z \sim 1.5$  ( $\sim 1.5$  Gyr), galaxies in the stellar mass range probed in the present work ( $M_* < 10^{11} M_{\odot}$ ) do not have enough time to consume their remaining gas reservoirs after the halt of cold gas accretion.

Sanders et al. (2018) showed that the MZR varies with SFR at  $z \sim 2.3$ , such that the gas-phase metallicity of galaxies at fixed  $M_*$  is anticorrelated with their SFRs. Using SED-derived SFRs, we also find slight evidence of enhanced SFR for star-forming galaxies located in overdensities. Therefore, the prominent gas accretion in overdense regions at high redshifts can explain both lower gas-phase metallicity and higher SFR of galaxies residing in overdensities at  $z \sim 2.3$ . It is worth noting that gas outflows can also play a significant role in lowering the gas-phase metallicity of galaxies located in overdensities and actively forming stars. These outflows can re-accrete into galaxies at lower redshifts and increase the gas-phase metallicity of galaxies as found in the present work at  $z \sim 1.5$ .

### 6. Summary

Using a large near-IR spectroscopic sample drawn from the MOSDEF survey, combined with the local density measurements from the CANDELS photometric survey, we study the environmental dependence of the MZR at  $z\sim1.5$  and  $z\sim2.3$ . We cross-match MOSDEF galaxies with the publicly available catalog of local density measurements in five CANDELS fields (Chartab et al. 2020) and use the N2 =  $\frac{[N \text{ II}]\lambda6584}{H\alpha}$  indicator to measure the gas-phase oxygen abundances of 167 galaxies at  $1.37 \leqslant z \leqslant 1.7$  and 303 galaxies at  $2.09 \leqslant z \leqslant 2.61$ .

The samples are labeled as overdense, intermediate density, and field based on their local density measurements. We matched the stellar mass distribution of our sample in three different environments to properly disentangle the effects of stellar mass from those related to the environment. Massive galaxies are mostly found in overdensities and unmatched underlying stellar mass distributions between different environments can affect the strength of the trends or even change the observed trends in the presence of a limited sample size. For the mass-matched sample, our findings can be summarized as follows:

1. At  $z\sim1.5$ , the average metallicity of galaxies in overdensities with  $M_*\sim10^{9.8}\,M_\odot$ ,  $10^{10.2}\,M_\odot$ , and  $10^{10.8}\,M_\odot$  is higher relative to their field counterparts by  $0.094\pm0.051$  ( $1.8\sigma$  significance),  $0.068\pm0.028$  ( $2.4\sigma$  significance), and  $0.052\pm0.043$  ( $1.2\sigma$  significance) dex, respectively. Also,

- the metallicity enhancements for  $M_* \sim 10^{9.8} M_{\odot}$  and  $10^{10.8} M_{\odot}$  galaxies in intermediate densities are  $0.090 \pm 0.052$  (1.7 $\sigma$  significance) and  $0.077 \pm 0.042$  (1.8 $\sigma$  significance) dex, respectively, and are insignificant for  $M_* \sim 10^{10.2} M_{\odot}$  galaxies.
- 2. At  $z \sim 2.3$ , galaxies that reside in overdensities with  $M_* \sim 10^{9.8} M_{\odot}$ ,  $10^{10.2} M_{\odot}$ , and  $10^{10.7} M_{\odot}$ , have a lower gas-phase metallicity by  $0.056 \pm 0.043$  ( $1.3\sigma$  significance),  $0.056 \pm 0.028$  ( $2\sigma$  significance), and  $0.096 \pm 0.034$  ( $2.8\sigma$  significance) dex compared to their coeval field sample, respectively. This metal deficiency is insignificant for galaxies residing in intermediate densities except for the massive galaxies ( $M_* \sim 10^{10.7} M_{\odot}$ ), for which we found  $0.085 \pm 0.034$  ( $2.5\sigma$  significance) dex metal deficiency compared to field counterparts.
- 3. Our results suggest that the efficient gas cooling mechanisms at high redshifts result in the prominent accretion of primordial metal-poor gas into the galaxies in overdensities. This cold metal-poor gas can dilute the metal content of ISM gas and lowers the gas-phase metallicity of galaxies, as seen in the present work ( $z \sim 2.3$ ). However, as galaxies evolve to the lower redshifts ( $z \le 2$ ), the shockheated gas in overdensities with massive halos cannot cool down efficiently, which prevents it from accreting into the galaxy. The termination of pristine gas accretion in overdensities, along with the accretion of preprocessed gas due to the strong outflows, increases the metallicity of galaxies at lower redshifts, z < 2. This scenario can explain our result at  $z \sim 1.5$ , where we find a metallicity enhancement for galaxies in overdensities compared to that for coeval field galaxies.

We thank the anonymous referee for providing insightful comments and suggestions that improved the quality of this work. We acknowledge support from NSF AAG grants AST-1312780, 1312547, 1312764, and 1313171, archival grant AR-13907 provided by NASA through the Space Telescope Science Institute. I.S. is supported by NASA through the NASA Hubble Fellowship grant #HST-HF2-51420, awarded by the Space Telescope Science Institute, which is operated by the Association of Universities for Research in Astronomy, Inc., for NASA, under contract NAS5-26555. The authors wish to extend special thanks to those of Hawaiian ancestry on whose sacred mountain we are privileged to be guests. Without their generous hospitality, most of the observations presented herein would not have been possible.

# Appendix A The MZR with [N II] $\lambda$ 6584 Detection Requirement

We perform linear regression for individual galaxies (nonstacked) to calculate the best-fit MZR for galaxies with a significant detection (S/N >3) in [N II]  $\lambda$ 6584. We note that requiring a detection in [N II]  $\lambda$ 6584 introduces a bias to our sample toward higher gas-phase metallicities, especially in the low-mass end of the MZR where nondetections are prevalent; however, it is worth investigating the offset between the best-fit MZRs in different environments without considering the contribution of [N II]  $\lambda$ 6584 nondetections. We fit a linear model,  $12 + \log(O/H) = Z_0 + \alpha[\log(M_*/M_{\odot}) - 10]$ , to the MZR of the samples in two extreme environment bins (underdensity and overdensity) considering both measurement errors in stellar mass and gas-phase metallicity. Figure A1

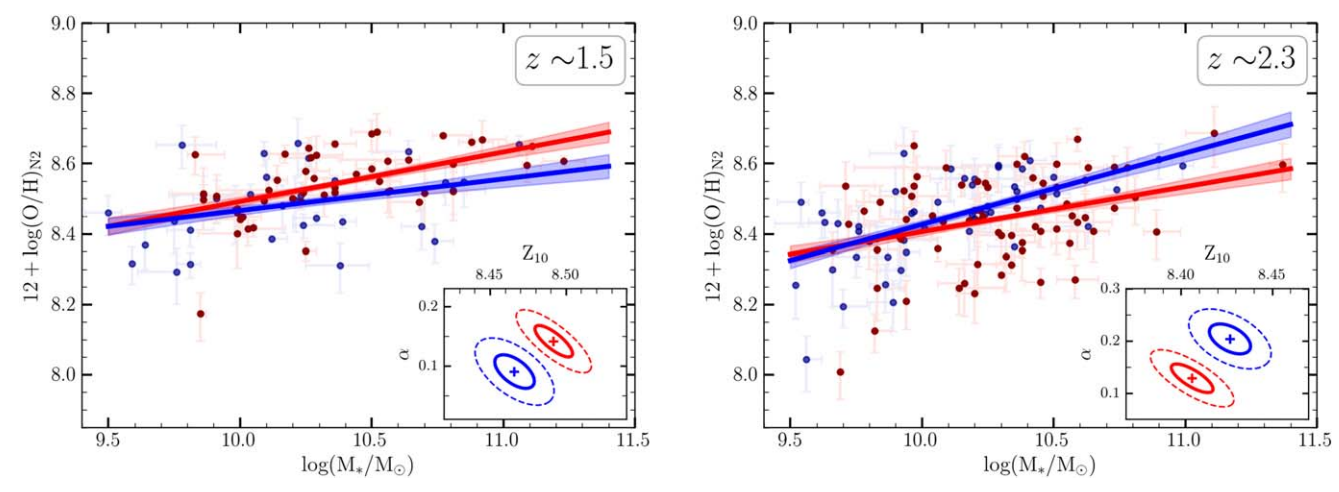


Figure A1. Similar to Figure 4, but here we ignore [N II]  $\lambda$ 6584 nondetection galaxies. The best-fit lines to MZRs are shown for galaxies with an S/N >3 detection in [N II]  $\lambda$ 6584, residing in two extreme environments, overdensity (red) and underdensity (blue). The shaded regions around the best-fit models show  $1\sigma$  error in the best-fit lines. Both gas-phase metallicity and stellar mass errors are taken into account in the regression analysis. Subpanels show the best value ("+"),  $1\sigma$  (solid), and  $2\sigma$  (dashed) confidence intervals for the two-dimensional posterior distribution of the slope and the intercept, which are considered to be free parameters of the linear model,  $12 + \log(O/H) = Z_0 + \alpha[\log(M_*/M_\odot) - 10]$ .

shows the best-fit lines along with 2D-posterior distributions of the slope and the intercept for the bins of environment. A significant distinction ( $>2\sigma$ ) between the posterior of fit parameters for the field galaxies and those located in overdensities suggests that the metallicity is enhanced at  $z \sim 1.5$  and suppressed at  $z \sim 2.3$  for galaxies in overdensities compared to field counterparts. Based on the best-fit models and their corresponding uncertainties, on average, galaxies in overdensities at  $z \sim 1.5$  have  $0.050 \pm 0.024$  dex higher gasphase metallicity compared to coeval field galaxies. The trend reverses at higher redshift,  $z \sim 2.3$ , such that galaxies residing in overdensities are metal deficient by  $0.055 \pm 0.025$  dex compared to the field counterparts. These results are in general agreement with our findings using mass-matched stacked spectra (Figure 7). Moreover, we estimate the intrinsic scatter of the MZR ( $\sigma_{\rm int}$ ) in both extreme environments at  $z \sim 1.5$  and  $z \sim 2.3$ . We assume that the observed scatter ( $\sigma_{\rm obs}$ ) around the best-fit MZR is  $\sigma_{\text{obs}}^2 = \sigma_{\text{int}}^2 + \sigma_{\text{meas}}^2$ , where  $\sigma_{\text{meas}}$  is the average measurement uncertainty. We estimate that the intrinsic scatter of the MZR at  $z \sim 1.5$  ( $z \sim 2.3$ ) is 0.07 (0.07) and 0.07 (0.10) dex for the field galaxies and those residing in overdensities, respectively, which are consistent with the intrinsic scatter of  $z \sim 0$  MZR in different environments (Cooper et al. 2008). We note that, although ignoring [N II]  $\lambda 6584$  nondetections does not change our conclusions, the bias is evident in the low-mass end of the MZR by comparing best-fit lines in Figure A1 with gas-phase metallicities derived from mass-matched stacked spectra (Figure 7). Therefore, the stacking technique employed in Section 4 is the preferred method as it provides an unbiased MZR where the contribution of [N II]  $\lambda 6584$  nondetections are taken into account properly.

### ORCID iDs

Nima Chartab https://orcid.org/0000-0003-3691-937X Alice E. Shapley https://orcid.org/0000-0003-3509-4855 Irene Shivaei https://orcid.org/0000-0003-4702-7561 Ryan L. Sanders https://orcid.org/0000-0003-4792-9119 Alison L. Coil https://orcid.org/0000-0002-2583-5894 Mariska Kriek https://orcid.org/0000-0002-7613-9872 Naveen A. Reddy https://orcid.org/0000-0001-9687-4973

### References

Alcorn, L. Y., Gupta, A., Tran, K.-V., et al. 2019, ApJ, 883, 153 Ando, M., Shimasaku, K., & Momose, R. 2020, MNRAS, 496, 3169 Azadi, M., Coil, A., Aird, J., et al. 2018, ApJ, 866, 63 Azadi, M., Coil, A. L., Aird, J., et al. 2017, ApJ, 835, 27 Balogh, M. L., Gilbank, D. G., Muzzin, A., et al. 2017, MNRAS, 470, 4168 Balogh, M. L., McGee, S. L., Mok, A., et al. 2016, MNRAS, 456, 4364 Barro, G., Pérez-González, P. G., Cava, A., et al. 2019, ApJS, 243, 22 Behroozi, P. S., Wechsler, R. H., & Conroy, C. 2013, ApJ, 770, 57 Brooks, A. M., Governato, F., Booth, C. M., et al. 2007, ApJL, 655, L17 Calzetti, D., Armus, L., Bohlin, R. C., et al. 2000, ApJ, 533, 682 Chabrier, G. 2003, PASP, 115, 763 Chartab, N., Mobasher, B., Darvish, B., et al. 2020, ApJ, 890, 7 Chiang, Y.-K., Overzier, R. A., Gebhardt, K., & Henriques, B. 2017, ApJL, Chisholm, J., Tremonti, C., & Leitherer, C. 2018, MNRAS, 481, 1690 Coil, A. L., Aird, J., Reddy, N., et al. 2015, ApJ, 801, 35 Conroy, C., Gunn, J. E., & White, M. 2009, ApJ, 699, 486 Contini, E., Gu, Q., Ge, X., et al. 2020, ApJ, 889, 156 Cooper, M. C., Newman, J. A., Weiner, B. J., et al. 2008, MNRAS, 383, 1058 Cucciati, O., Zamorani, G., Lemaux, B. C., et al. 2014, A&A, 570, A16 Darvish, B., Mobasher, B., Sobral, D., et al. 2016, ApJ, 825, 113 Darvish, B., Scoville, N. Z., Martin, C., et al. 2020, ApJ, 892, 8 Dekel, A., & Birnboim, Y. 2006, MNRAS, 368, 2 Elbaz, D., Daddi, E., Le Borgne, D., et al. 2007, A&A, 468, 33 Ellison, S. L., Simard, L., Cowan, N. B., et al. 2009, MNRAS, 396, 1257 Erb, D. K., Shapley, A. E., Pettini, M., et al. 2006, ApJ, 644, 813 Finkelstein, S. L., Hill, G. J., Gebhardt, K., et al. 2011, ApJ, 729, 140 Fossati, M., Wilman, D. J., Fontanot, F., et al. 2015, MNRAS, 446, 2582 Fossati, M., Wilman, D. J., Mendel, J. T., et al. 2017, ApJ, 835, 153 Galametz, A., Grazian, A., Fontana, A., et al. 2013, ApJS, 206, 10 García-Portugués, E., Crujeiras, R. M., & González-Manteiga, W. 2013, J. Multivar. Anal., 121, 152 Garnett, D. R. 2002, ApJ, 581, 1019 Grogin, N. A., Kocevski, D. D., Faber, S. M., et al. 2011, ApJS, 197, 35 Guo, Y., Ferguson, H. C., Giavalisco, M., et al. 2013, ApJS, 207, 24

Gupta, A., Yuan, T., Torrey, P., et al. 2018, MNRAS, 477, L35

```
Heckman, T. M., Armus, L., & Miley, G. K. 1990, ApJS, 74, 833
Hennawi, J. F., Prochaska, J. X., Cantalupo, S., & Arrigoni-Battaia, F. 2015,
   Sci, 348, 779
Jackson, J. C. 1972, MNRAS, 156, 1P
Ji, Z., Giavalisco, M., Williams, C. C., et al. 2018, ApJ, 862, 135
Kacprzak, G. G., Yuan, T., Nanayakkara, T., et al. 2015, ApJL, 802, L26
Kawinwanichakij, L., Papovich, C., Quadri, R. F., et al. 2017, ApJ, 847, 134
Kereš, D., Katz, N., Weinberg, D. H., & Davé, R. 2005, MNRAS, 363, 2
Kewley, L. J., Dopita, M. A., Leitherer, C., et al. 2013, ApJ, 774, 100
Kewley, L. J., & Ellison, S. L. 2008, ApJ, 681, 1183
Kodra, D. 2019, PhD thesis, Univ. Pittsburgh
Koekemoer, A. M., Faber, S. M., Ferguson, H. C., et al. 2011, ApJS, 197, 36
Kriek, M., Shapley, A. E., Reddy, N. A., et al. 2015, ApJS, 218, 15
Kriek, M., van Dokkum, P. G., Labbé, I., et al. 2009, ApJ, 700, 221
Kulas, K. R., McLean, I. S., Shapley, A. E., et al. 2013, ApJ, 774, 130
Lemaux, B. C., Cucciati, O., Le Fèvre, O., et al. 2020, arXiv:2009.03324
Leung, G. C. K., Coil, A. L., Aird, J., et al. 2019, ApJ, 886, 11
Leung, G. C. K., Coil, A. L., Azadi, M., et al. 2017, ApJ, 849, 48
Lilly, S. J., Carollo, C. M., Pipino, A., Renzini, A., & Peng, Y. 2013, ApJ,
   772, 119
Maier, C., Hayashi, M., Ziegler, B. L., & Kodama, T. 2019, A&A, 626, A14
Maiolino, R., & Mannucci, F. 2019, A&ARv, 27, 3
Mannucci, F., Cresci, G., Maiolino, R., et al. 2009, MNRAS, 398, 1915
Mannucci, F., Cresci, G., Maiolino, R., Marconi, A., & Gnerucci, A. 2010,
          S. 408, 2115
Martin, C. L., Shapley, A. E., Coil, A. L., et al. 2012, ApJ, 760, 127
McGee, S. L., Bower, R. G., & Balogh, M. L. 2014, MNRAS, 442, L105
McLean, I. S., Steidel, C. C., Epps, H. W., et al. 2012, Proc. SPIE, 8446,
Momcheva, I. G., Brammer, G. B., van Dokkum, P. G., et al. 2016, ApJS,
  225, 27
Mouhcine, M., Baldry, I. K., & Bamford, S. P. 2007, MNRAS, 382, 801
Muldrew, S. I., Hatch, N. A., & Cooke, E. A. 2015, MNRAS, 452, 2528
Mushotzky, R. F., & Loewenstein, M. 1997, ApJL, 481, L63
Muzzin, A., Marchesini, D., Stefanon, M., et al. 2013, ApJ, 777, 18
Namiki, S. V., Koyama, Y., Hayashi, M., et al. 2019, ApJ, 877, 118
Nantais, J. B., Muzzin, A., van der Burg, R. F. J., et al. 2017, MNRAS,
   465, L104
```

```
Nayyeri, H., Hemmati, S., Mobasher, B., et al. 2017, ApJS, 228, 7
Old, L. J., Balogh, M. L., van der Burg, R. F. J., et al. 2020, MNRAS,
  493, 5987
Peng, Y.-j., & Maiolino, R. 2014, MNRAS, 438, 262
Pettini, M., & Pagel, B. E. J. 2004, MNRAS, 348, L59
Pintos-Castro, I., Yee, H. K. C., Muzzin, A., Old, L., & Wilson, G. 2019, ApJ,
  876, 40
Reddy, N. A., Kriek, M., Shapley, A. E., et al. 2015, ApJ, 806, 259
Sanders, R. L., Shapley, A. E., Kriek, M., et al. 2015, ApJ, 799, 138
Sanders, R. L., Shapley, A. E., Kriek, M., et al. 2018, ApJ, 858, 99
Sanders, R. L., Shapley, A. E., Reddy, N. A., et al. 2020, MNRAS, 491, 1427
Schaefer, A. L., Tremonti, C., Pace, Z., et al. 2019, ApJ, 884, 156
Shapley, A. E., Sanders, R. L., Shao, P., et al. 2019, ApJL, 881, L35
Shimakawa, R., Kodama, T., Tadaki, K.-i., et al. 2015, MNRAS, 448, 666
Shivaei, I., Kriek, M., Reddy, N. A., et al. 2016, ApJL, 820, L23
Shivaei, I., Reddy, N. A., Siana, B., et al. 2018, ApJ, 855, 42
Shivaei, I., Reddy, N. A., Steidel, C. C., & Shapley, A. E. 2015, ApJ, 804,
Skelton, R. E., Whitaker, K. E., Momcheva, I. G., et al. 2014, ApJS, 214, 24
Sobral, D., Smail, I., Best, P. N., et al. 2013, MNRAS, 428, 1128
Spitler, L. R., Labbé, I., Glazebrook, K., et al. 2012, ApJL, 748, L21
Stefanon, M., Yan, H., Mobasher, B., et al. 2017, ApJS, 229, 32
Steidel, C. C., Erb, D. K., Shapley, A. E., et al. 2010, ApJ, 717, 289
Steidel, C. C., Rudie, G. C., Strom, A. L., et al. 2014, ApJ, 795, 165
Stocke, J. T., Danforth, C. W., Shull, J. M., Penton, S. V., & Giroux, M. L.
  2007, ApJ, 671, 146
Stott, J. P., Sobral, D., Bower, R., et al. 2013, MNRAS, 436, 1130
Tran, K.-V. H., Nanayakkara, T., Yuan, T., et al. 2015, ApJ, 811, 28
Tran, K.-V. H., Papovich, C., Saintonge, A., et al. 2010, ApJL, 719, L126
Tremonti, C. A., Heckman, T. M., Kauffmann, G., et al. 2004, ApJ, 613, 898
Valentino, F., Daddi, E., Strazzullo, V., et al. 2015, ApJ, 801, 132
van de Voort, F., Bahé, Y. M., Bower, R. G., et al. 2017, MNRAS, 466, 3460
van de Voort, F., & Schaye, J. 2012, MNRAS, 423, 2991
Wu, P.-F., Zahid, H. J., Hwang, H. S., & Geller, M. J. 2017, MNRAS,
  468, 1881
Yuan, T., Nanayakkara, T., Kacprzak, G. G., et al. 2014, ApJL, 795, L20
Zahid, H. J., Dima, G. I., Kudritzki, R.-P., et al. 2014, ApJ, 791, 130
Zavala, J. A., Casey, C. M., Scoville, N., et al. 2019, ApJ, 887, 183
```